



Article

# Toward Converged Satellite/Fiber 1550 nm DS-BB84 QKD Networks: Feasibility Analysis and System Requirements

Aristeidis Stathis <sup>\*</sup>, Argiris Ntanos, Nikolaos K. Lyras, Giannis Giannoulis , Athanasios D. Panagopoulos  and Hercules Avramopoulos

School of Electrical and Computer Engineering, National Technical University of Athens, 9 Iroon Polytechnique Str., 15780 Athens, Greece; ntanosargiris@mail.ntua.gr (A.N.); lyrasnikos@mail.ntua.gr (N.K.L.); jgiannou@mail.ntua.gr (G.G.); thpanag@ece.ntua.gr (A.D.P.); hav@mail.ntua.gr (H.A.)

<sup>\*</sup> Correspondence: stathisaris@mail.ntua.gr; Tel.: +30-21-0772-2057

**Abstract:** Satellite-based QKD is currently being developed to revolutionize global cryptographic key exchange by facilitating secure communication among remote parties at a global scale. By overcoming the exponential loss of fiber transmission, satellite-to-Earth communication can seamlessly interconnect vast distances as the link budget of such links is sufficient to support QKD links. In terms of this direction, DV-QKD implementations seems to be technologically ahead since key exchange has been experimentally demonstrated to perform much more efficiently by providing key rates that are orders of magnitude higher compared to entanglement-based key exchange. However, the specific requirements to support effectively functional DV-QKD satellite-to-ground links are yet to be defined. This work attempts to define the satellite and ground segment system requirements needed in order to achieve functional QKD service for various satellites orbits (LEO, MEO, and GEO). Finite key size effects are being considered to determine the minimum block sizes that are required for secure key generation between a satellite node and a ground terminal for a single satellite pass. The atmospheric link channel is modeled with consideration of the most important degradation effects such as turbulence and atmospheric and pointing loss. Critical Tx and Rx system parameters, such as the source's intrinsic Quantum Bit Error Rate (iQBER), the Rx telescope aperture size, and detection efficiency, were investigated in order to define the minimum requirements to establish an operation satellite-to-ground QKD link under specific assumptions. The performance of each downlink scenario was evaluated for the wavelength of 1550 nm in terms of link availability, link budget, and in the distilling of secure key volumes over time. Finally, the feasibility and requirements for distributing the collected space photons via terrestrial telecom fibers was also studied and discussed, leading to the proposal of a more futuristic WDM-enabled satellite QKD architecture. This comprehensive analysis aims to contribute to the advancement and implementation of effective satellite-based QKD systems, which can further exploit the ground fiber segment to realize converged space/terrestrial QKD networks.

**Keywords:** satellite-to-ground QKD; DV-QKD; finite key size; LEO; MEO; GEO; space/terrestrial quantum communication infrastructure (QCI)



**Citation:** Stathis, A.; Ntanos, A.; Lyras, N.K.; Giannoulis, G.; Panagopoulos, A.D.; Avramopoulos, H. Toward Converged Satellite/Fiber 1550 nm DS-BB84 QKD Networks: Feasibility Analysis and System Requirements. *Photonics* **2024**, *11*, 609. <https://doi.org/10.3390/photonics11070609>

Received: 9 May 2024  
Revised: 17 June 2024  
Accepted: 24 June 2024  
Published: 27 June 2024



**Copyright:** © 2024 by the authors. Licensee MDPI, Basel, Switzerland. This article is an open access article distributed under the terms and conditions of the Creative Commons Attribution (CC BY) license (<https://creativecommons.org/licenses/by/4.0/>).

## 1. Introduction

Over the past hundred years, significant advances in quantum mechanics, optics, computing, and information theory have paved the way for a new era in quantum technologies. This emerging “second quantum revolution” builds on the initial explorations into quantum mechanics to harness these principles for revolutionary applications across various sectors. One of the most groundbreaking and forward-looking developments is the concept of the quantum Internet [1]. Since the exponential increase in signal losses in fiber-optic cables over long distances currently hinders the reliable transmission of quantum states beyond a few hundred kilometers [2], and as the current state of quantum memories and quantum

repeaters faces a great deal of open questions [3] beyond practical deployments, there is an ambitious goal to establish a worldwide sophisticated network that should include satellites. This network will connect quantum computers, repeaters, and storage devices through both classical and quantum channels, where satellite nodes will communicate over quantum channels with terrestrial nodes, and distributed quantum computers will also connect around the world for unconditionally safe communication [4]. Such a network promises to revolutionize fields by enabling distributed quantum computing [5], secure quantum communication [6], enhanced imaging techniques [7], and improved precision in timing [8], among other potential benefits. Progress toward this vision includes the seminal experiments of the Micius satellite, which performed quantum communication between a satellite and the Earth, demonstrating Quantum Key Distribution (QKD) [9–12], entanglement distribution [13], and quantum teleportation [14].

In recent years, the landscape of quantum communication and QKD has seen a growing interest worldwide, with several countries launching funding and implementation initiatives for satellite-based QKD research projects. This growing interest is justified by the plethora of scientific papers and infrastructure mission projects that highlight the stages of research, development, and the demonstration of technology. Notably, in Europe, significant strides are being made through collaborative efforts between the European Commission (EC), the European Space Agency (ESA), and various European space companies, which are exemplified by missions such as Eagle-1 [15]. This mission not only includes a QKD system, but also marks a transition from experimental demonstrations to operational service provision, and its launch is scheduled for 2025. Similarly, the SAGA 1G mission [16] represents the first generation of the European Quantum Communication Infrastructure's (EuroQCI) space segment, where the aim is for in-orbit validations of the QKD performance and system verification by 2027. Further enriching the European QKD landscape are the IRIS2 [17] and QUBE-II [18] missions. IRIS2 is envisioned as a future generation of the EU Secure Satellite Constellation, integrating EuroQCI and thereby enhancing resilience, interconnectivity, and security through satellite technology. QUBE-II, on the other hand, is a CubeSat mission equipped with two distinct BB84 Prepare and Measure (P&M)-QKD systems, and it is designed for LEO downlink experimental demonstration, with its launch also being anticipated in 2025. These initiatives, including the EC's EuroQCI and the ESA's SAGA mission underscore a concerted effort toward establishing a comprehensive network of satellite quantum communication systems. This effort is further supported by the inclusion of a terrestrial backbone component, which comprises fiber networks in major cities [19–23], thereby creating a synergistic space-ground quantum communication infrastructure.

International projects like Canada's QEYSSat project [24] and the UK's QUARC [25], as well as Singaporean missions like SpooQy [26] and QUICK3 [27], are also reinforcing the global drive to advance quantum communication technologies. More specifically, the QEYSSat mission stands out for its unique approach in employing an uplink method to test the BB84 and BBM92 protocols, diverging from the common practice in other missions. The UK's QUARC mission focuses on providing secure satellite QKD service to the UK via a constellation of CubeSats, while Singaporean space mission projects are also considered among the most mature with seminal demonstrations from the SpooQy-1 CubeSat mission, which demonstrated polarization-based quantum entanglement correlations. Additionally, the ongoing QUICK<sup>3</sup> mission aims to design a compact, true, and single-photon source that can enhance the secure data rates in satellite-based QKD scenarios when compared to conventional laser-based light sources.

In parallel to these important milestones for satellite-QKD networks, the quantum engineering community is advancing space-based QKD technologies to deliver improvements in Key Performance Indicators (KPIs) for higher Secure Key Rates (SKR), innovations in space-QKD components for new system designs and architectures, and preparations for the future quantum space Internet [28]. The initial efforts to optimize the performance of satellite QKD downlinks are focusing on the design and development of state-of-the-art

GHz on-board sources [29–32], with improved KPIs and Size, Weight, and Power (SWAP) parameters. Alongside hardware advancements, there is significant theoretical work on the precise modeling of atmospheric channel [33–38] network optimization [39,40] and security considerations, including finite key size analysis [41] for satellite-to-ground QKD communications. Efforts are also underway to upgrade Optical Ground Stations (OGS) to be quantum-ready [42,43], with technologies like Adaptive Optics (AO) systems and advanced free-space-to-fiber coupling techniques [44] being developed to optimize the integration of space- and ground-based infrastructures. Additionally, high-detection efficiency systems are being investigated to augment the OGS [45]; however, their deployment is constrained by factors such as bulkiness, the availability of cooling technologies, and cost considerations. These kinds of technologies would optimize the coupling performance, thus enabling the connection between the space segment and the terrestrial, fiber-based infrastructures.

Amidst the advances in satellite-based QKD and the establishment of quantum communication infrastructures, there remains a need for studies and system designs that will bridge the terrestrial and space segments of QCI. This necessity underscores the importance of developing networks that seamlessly combine space and fiber technologies. This is where this research contribution stands. The contribution of this study lies in its methodology for determining the essential requirements for a given set of assumptions to achieve satellite QKD, where the aim is to bridge the fiber infrastructure and space-QCI segment, thus addressing a critical gap in the current research and development ecosystem. Our research also aims to open the door to the design phase of converged space/terrestrial QKD networks, thus leveraging the mature architecture design options for terrestrial distribution topologies and the KPIs provided by the future highly efficient, GHz-scale, and robust satellite P&M QKD downlinks.

The remainder of this paper is structured as follows: Section 2 introduces the envisioned architecture, providing the foundational concepts and systems assumptions that underpin this work. Section 3 delves into the specifics of the software tool developed and utilized for this research, where the details of the satellite-to-ground QKD link modeling are presented. In Section 4, the results are presented, where a top-down approach is adopted. This strategy aims to consider the full spectrum of options for satellite-based QKD downlinks by assessing their potential and limitations across different operational contexts. After this initial consideration, the approach, based on specific criteria or considerations such as technical feasibility or the specific requirements of quantum communication technologies, involves narrowing down the choices by progressively focusing on certain orbits that favor the satellite-to-ground QKD in terms of secure key generation. Following this analytical framework, Section 5 shifts focus toward a more forward-looking perspective, where the future possibilities of satellite-based QCI are discussed by leveraging state-of-the-art specifications from both the space and ground segments. This section aims to give a rough idea of the full potential of each orbit, considering state-of-the-art parameters that could redefine the capabilities of quantum communications infrastructure. Finally, Section 6 concludes this work.

## 2. System Architecture and Assumptions

Driven by already conducted experimental demonstrations, our analysis will be focused on the Discrete Variable (DV)-QKD systems. DV-QKD implementations seem to be technologically ahead since key exchange has been experimentally demonstrated to perform much more efficiently, providing key rates that are orders of magnitude higher compared to entanglement-based key exchange [37]. We selected for our analysis the prepare-and-measure (one-way) scheme and the BB84 protocol with decoy and vacuum states (vacuum, decoy, and signal). DS-BB84 QKD is the best understood and most widely studied scheme and protocol, and it also has the advantage that complete general security proofs are available, which have also been widely scrutinized for correctness [46]. Moving on to the system architecture, satellites across all the operational orbits, i.e., Low Earth Orbit (LEO), Medium Earth Orbit (MEO), and Geostationary Earth Orbit (GEO) will be

examined. We will investigate their possible limitations, but also their potential use and advantages. Satellites in LEO can be considered a prominent choice due to the reduced geometrical losses that occur due to beam diffraction when compared to the other two orbits, as well as the increased market interest and the everyday increasing number of LEO satellites that are launched. On the other hand, satellites in MEO may be an attractive alternative, especially for locations close to the equator as they offer a larger visibility time window per satellite, thus resulting in a need for shorter satellite constellations to achieve a continuous communication (with at least one satellite at a time in contrast to the LEO case). The penalty for this case is the increased free-space losses in contrast with LEO, but also the resulting low elevation angles for locations far from the equator. Finally, GEO satellites can offer continuous communication employing a single satellite. However, the high altitude results in much higher losses, making the establishment of the quantum link challenging. At this point, it is important to note that our analysis is limited to the downlink scenario to avoid the challenges associated with lossy and turbulent uplink transmission [47,48]. For satellite QKD systems, there are two principal wavelength regimes that are considered as possible candidates, namely wavelengths in the low end of the near-infrared (NIR) band, i.e., 810–850 nm, and wavelengths near the low end of the short-wave infrared (SWIR) band, i.e., C-telecom band (1530–1565 nm). Comparing the choice of 850 nm versus the telecom C-band for QKD channel in satellite-to-ground links presents a nuanced trade-off between atmospheric conditions, signal-to-noise (S/N) ratio, and technological compatibility. Operating at an 850 nm wavelength can significantly enhance the S/N probabilities and qubit-transmission rates for satellite-to-ground communications. This advantage stems from a combination of higher photon energy, reduced field-of-view (FOV) requirements, and better aperture coupling efficiency when compared to longer wavelengths. MODTRAN simulations suggest that local sky radiances are considerably higher at 850 nm; yet, the noise photon count remains manageable due to the higher photon energy and smaller FOV. The atmospheric transmission at this wavelength is also quite high, reaching about 90% of that observed at 1550 nm. Importantly, the near-visible wavelength of 850 nm permits the use of efficient, compact, and cost-effective silicon-based detectors.

On the other hand, the telecom C-band around 1550 nm is recognized for its slightly higher atmospheric transmission efficiency and significantly lower solar noise interference, which are attributed to the inherent properties of Rayleigh scattering and the relative weakness of sunlight intensity at this wavelength. The choice of 1550 nm also benefits from a substantial reduction in background noise, making it a quieter channel for QKD. Moreover, the compatibility of 1550 nm with existing fiber-optical communication infrastructure makes it an appealing choice as it facilitates seamless integration between satellite-based and terrestrial quantum communication networks.

Ultimately, the decision between these wavelengths should consider site-specific conditions, including atmospheric scattering and turbulence, as well as the technological ecosystem surrounding the quantum communication infrastructure. While 850 nm offers superior S/N ratios and allows for the use of more accessible detection technologies, 1550 nm provides a more robust channel and easier integration with existing communication systems. The optimal wavelength for a specific satellite-to-Earth QKD link would thus depend on a balance of these factors, where the aim is to maximize both the efficiency and the practicality of the quantum communication channel.

Although, up to now, the majority of the satellite QKD links operating in the regime of 850 nm are motivated mainly by the responsivity of silicon-based Single-Photon Avalanche Diodes (SPADs) in this regime and the presence of fewer geometrical losses (almost four-times greater) [49], our analysis will be focused on the 1550 nm regime. The employment of telecom wavelengths provides the benefit of a direct coupling into an SMF, thus enabling the detection of the quantum signal beyond the telescope to a remote location, as well as the capability of using advanced commercial off-the-shelf optical fiber components for the realization of the filtering, classical and quantum signal separation, and polarization encoding analysis. In addition, according to MODTRAN, the transmission efficiency is



slightly higher at 1550 nm than at 850 nm, and the background noise, which is present mainly due to sunlight/moonlight, is reduced. In this direction, the feasibility and requirements for distributing the collected space photons via terrestrial telecom fibers is also being studied with respect to the integration of space QKD segments with the terrestrial ground fiber-based QCI segments. Figure 1 provides a schematic overview of the envisioned architecture, where OGSs can be located outside from the terrestrial grid, thus allowing one to take advantage of the high-altitude locations, where there is less artificial background noise, and the effect of turbulence is also reduced. In this way, photons can be transferred from the OGS to the urban environment via advanced low-loss telescope-to-fiber coupling techniques, thus removing the need for the detection of the collected photons in the OGSs and an intermediate trusted node.

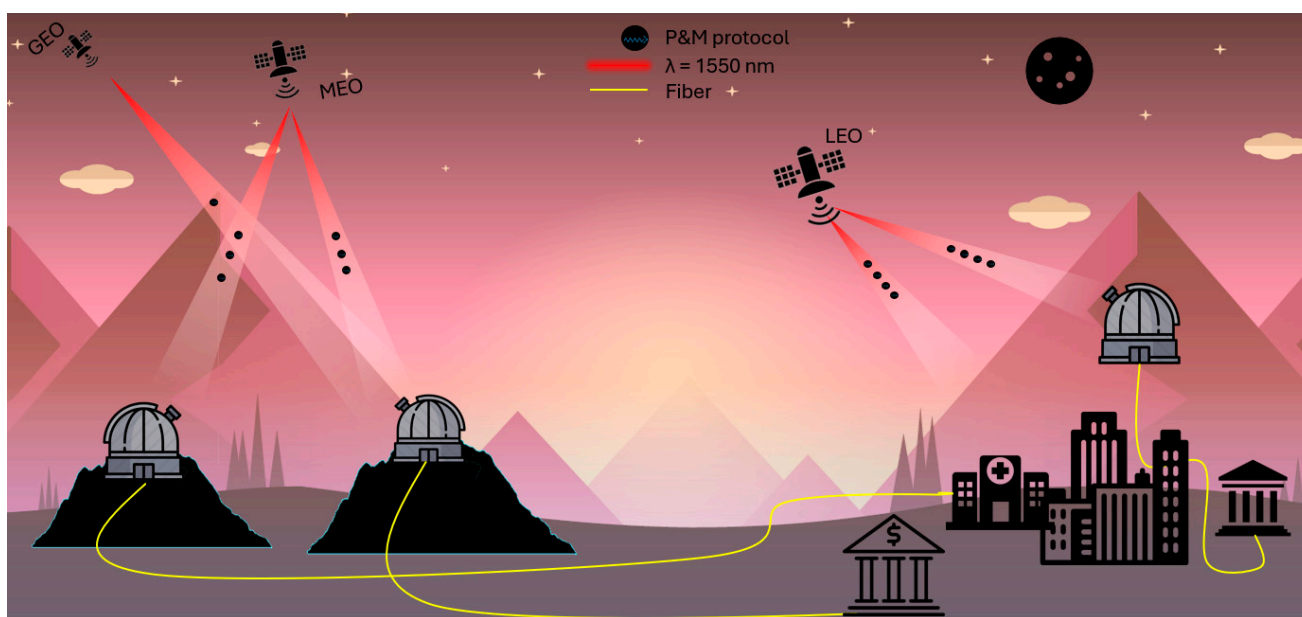


**Figure 1.** Schematic of the envisioned architecture integrating urban and terrestrial grid networks across LEO, MEO, and GEO orbits for DS-BB84 QKD downlinks under night-time conditions. The fiber distribution routes from OGS to detection stations are illustrated with yellow lines.

In the following section, the assumptions underpinning our study are presented. To streamline our simulation process and ensure a focused analysis, we utilized the specific technological and operational parameters defined by the Micius mission as our baseline scenario [50]. By leveraging the established specifications of the Micius mission as a benchmark, we adhere to proven parameters, which can enhance the relevance and applicability of the findings provided by our simulation. For example, we kept, throughout our simulation process, the aperture emitter constant to 30 cm, so unless stated otherwise, these will be the baseline parameters used in our simulation.

### 2.1. Orbits

The orbit parameter is one of the most crucial parameters since it decides the visibility of each satellite with the OGSs considered in the system architecture, as depicted in Figure 1. Initially, satellites across all operational orbits, i.e., LEO, MEO, and GEO are considered. This strategy aims to consider the full spectrum of options for satellite-based quantum communications by assessing their potential and limitations across different operational contexts. For the case of LEO and MEO satellites, the elevation and range of the satellite-OGS channel are calculated as a function of time for different satellite overpasses.

## 2.2. Receiving Terminal

We started by considering the Micius receiving characteristics. We, thus, started by considering a receiving aperture diameter of 1 m, with a focal length of 10 m and an obscuration ratio of 0.1, which was located at an 850 m altitude (as was the OGS in Xinglong). Moving forward, our study will focus on employing telescopes with diverse design parameters (such as aperture diameter, obscuration ratio, focal length, etc.) as receivers by varying the parameters crucial for establishing communication in the photon starve regime. Fiber coupling will also be considered by modeling the coupling efficiency in terms of Strehl ratio metrics.

The choice between Superconducting Nanowire Single-Photon Detectors (SNSPDs) and SPADs for signal detection is pivotal given their distinct operational characteristics. Focusing our attention on 1550 nm, we explored the potential of establishing robust quantum communication links by employing both SNSPDs and SPADs for signal detection. SNSPDs are acknowledged for their superior quantum efficiency across a broad wavelength range, albeit with higher complexity and cost due to the necessitated cryogenic cooling. Conversely, SPADs present a more cost-effective solution, albeit with certain limitations in detection efficiency and timing jitter.

## 2.3. OGS-to-Detection Station Fiber Distribution

In this study, telescope-to-fiber coupling, which enables signal transmission over extended distances through low-loss, single-mode optical fibers to a secure location for detection (which may be in a different location with respect to the receiving telescope), was also modeled. In this way, it was not necessary to upgrade the security of the OGS to a trusted-node configuration, which would have stressed the overall security of the networks. This free-space and fiber-integrated hybrid QKD transmission scenario was recently successfully demonstrated using fiber-connected measurement terminals equipped with SNSPDs [51]. This approach allows not only for the detectors to be safely enclosed in a different room or building, but it also enables multiple users to utilize the same optical telescope. Additionally, fiber coupling may allow for an OGS to be located in favorable locations and outside the urban grid, as well as grant higher altitudes, lower aerosol concentrations, and reduce artificial background noise, while also enabling the extension of the satellite QKD downlink to the urban areas without the need of an intermediate trusted node at the OGS site.

## 3. Satellite-to-Ground QKD Simulator

In this section, we provide an in-depth description of the mathematical framework of the developed satellite-to-ground QKD simulator software (MTLAB 2020). To provide a clear understanding of our software's features, we categorize its functionalities into three main areas. The first area focuses on the space segment where the satellite resides. The initial step involves the calculation of elevation angle over time. For this estimation, we used the latitude, longitude, and orbital height data of each satellite, which are obtained every 10 s when employing the AGI/STK system tool (ANSYS, Pittsburgh, PA, USA) [52]. For simplicity, in this study, only a satellite pass was modeled. Considerations such as the specifications of the transmitter and receiver enable calculations of the geometrical loss, the pointing losses, and the receiving system loss (such as in telescope-to-SMF couplings). Next, we delved into atmospheric channel modeling, which accounts for all the atmospheric phenomena such as turbulence and atmospheric absorption that degrade the link's performance. Finally, the Decoy-State BB84 DV-QKD protocol was utilized, including finite key size analysis. Overall, by modeling the abovementioned protocols and methods, the software was able to provide metrics such as the SKR, Quantum Bit Error Rate (QBER), and link budget estimations. Above, a flow chart illustrates the simulation process (Figure 2). Inputs are marked in green squares, outputs in orange, and the simulation steps are highlighted in blue boxes, thus providing a visual guide through our simulation methodology.

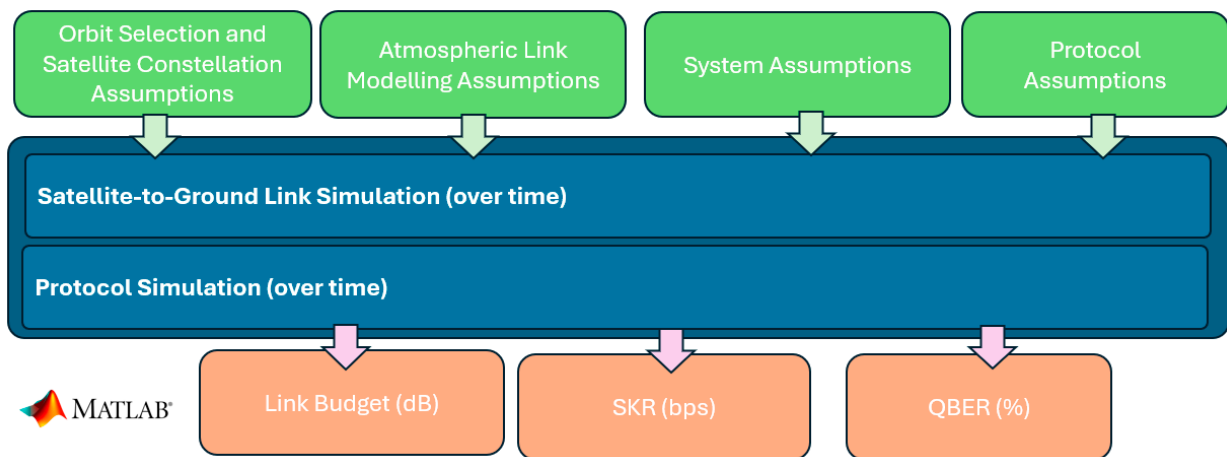


**Figure 2.** Flow chart of the satellite-to-ground MATLAB 2020 software calculator.

### 3.1. Satellite Orbits

Our software tool can simulate a comprehensive range of orbits, including LEO, MEO, and GEO, thus ensuring a versatile application for diverse QKD–satellite mission analyses.

LEO satellite orbits are characterized by their relatively low altitudes, typically within 2000 km above the Earth’s surface, thus providing a better link budget for the QKD downlinks and enabling higher key rates. The low orbits enable satellites to complete one orbit around the Earth in approximately 90 to 120 min, thus resulting in frequent communication time windows as they pass overhead. Specifically, for Sun Synchronous Orbits (SSOs), the satellites are visible approximately every 12 h with the same elevation gained by an OGS. Finally, LEO satellites offer global coverage but require constellations of multiple satellites to provide continuous service. Therefore, it is of great importance to consider whether a single LEO satellite pass provides an adequate volume of exchanged bits for post processing when finite key size statistical fluctuations are being considered.

MEO satellite orbit altitudes typically range between 2000 and 35,786 km. MEO satellites orbit the Earth less frequently than their LEO counterparts, typically completing one orbit every several hours, thus resulting in fewer communication opportunities per day. While MEO satellites provide broader coverage than LEO satellites, their elevation gain strongly depends on the OGS location since most MEO constellations fly across the equator. The trade-off between longer communication time windows and a lower link budget will be considered in the following section in terms of finite key size statistical fluctuations.

Finally, GEO satellites are located 36,000 km above the Earth’s surface. Since they move at the same angular speed as the Earth, they appear to not be moving in respect to an OGS, thus allowing for continuous communication.

### 3.2. Atmospheric Link Modeling

#### 3.2.1. Geometrical Loss

Geometrical loss is a primary factor affecting the link budget in space-based quantum communication, and it increases quadratically with distance. For a satellite orbiting in LEO/MEO, the distance between the satellite and the ground depends on the satellite’s elevation angle and can be computed using Equation (1).

$$d(\theta) = R_e \left( \sqrt{\left( \frac{H + R_e}{R_e} \right)^2 - \cos^2 \theta} - \sin \theta \right), \tag{1}$$

where  $H$  is the satellite’s altitude above the Earth’s surface,  $R_e$  is the Earth’s radius, and  $\theta$  is the elevation angle. The geometrical loss factor can then be calculated using (2) according to [53]:

$$A_{geo} = \left( \frac{\lambda}{4\pi d(\theta)} \right)^2 \times \left( \frac{\pi D_r}{\lambda} \right)^2 \times \left( \frac{8}{\theta_B^2} \right), \tag{2}$$

where  $D_r$  is the receiving aperture diameter and  $\theta_B$  is the half-width divergence angle of the transmitted beam, which assumes a Gaussian beam profile.

### 3.2.2. Pointing Loss

The necessity for a narrow beam width makes accurate pointing acquisition critical. The inaccurate point acquisition of the laser beam renders the receiver to be located off-axis from the far-field irradiance profile, resulting in a pointing loss. Pointing errors cause time-varying fading in the received signal power. They can be estimated for a specific probability from the Probability Density Function (PDF) of a normalized received intensity by taking into account the pointing error in the same manner as conducted in [54].

$$p(I_{pp}) = \beta_p \bar{I}_{pp}^{\beta_p - 1}, \quad 0 \leq I_{pp} \leq 1, \tag{3}$$

where  $I_{pp} = \frac{\beta_p}{\beta_p + 1}$  and  $\beta_p = \frac{\theta_B^2}{4} \sigma_p^2$  is the divergence pointing ratio, with  $\theta_B$  defined as previously, and  $\sigma_p$  is the pointing error variance in radians. The total pointing error loss for a specific outage probability  $p_0$  was calculated using the following expression [54]:

$$L_{pt} = p_0^{1/\beta_p}. \tag{4}$$

### 3.2.3. Atmospheric Transmission

Atmospheric transmission involves the interaction of photons with atmospheric constituents, thus leading to signal attenuation, scattering, and degradation. The transmittance varies with the satellite’s elevation angle, and it can be calculated under clear sky conditions using the following formula [55]:

$$L_a = L_{zen}^{\left(\frac{1}{\cos(\zeta)}\right)}, \tag{5}$$

where  $L_{zen}$  is the transmittance for a vertical link at a specific wavelength and  $\zeta$  is the zenith angle of the link. It is evident that, for low elevation angles, atmospheric attenuation is higher since the light must travel a longer path through the atmosphere to reach the receiver.

### 3.2.4. Turbulence

Scintillation effects on Free Space Optical (FSO) communication links can cause signal intensity fluctuations. These fluctuations result from thermal changes by affecting refractive indices, thus leading to beam diffraction. Turbulence-induced scintillation is categorized based on the refractive index structure parameter  $C_n^2$  ( $\text{m}^{-2/3}$ ). The value of this parameter is largely dependent on atmospheric conditions such as temperature and pressure. This study used the modified expression of the Hufnagel–Valley model [53], which considers the altitude of the ground station and the elevation angle of the link.

$$C_n^2(h) = A_0 \exp\left(-\frac{H_{GS}}{700}\right) \exp\left(\frac{H_{GS} - h}{100}\right) 5.94 \times 10^{-53} \left(\frac{u_{rms}}{27}\right)^2 h^{10} \exp\left(-\frac{h}{1000}\right) + 2.7 \times 10^{-16} \exp\left(-\frac{h}{1500}\right). \tag{6}$$

The calculation of the refractive index structure parameter  $C_n^2$  ( $\text{m}^{-2/3}$ ) requires integrating the average wind speed  $u_{rms}$  (m/s) along the slant path by employing the Bufton model [56], as well as by accounting the altitude of the ground station  $H_{GS}$  (m) and the height above the ground station  $h$  (m). The scintillation index for weak, average, and strong



turbulence, when assuming a plane wave approximation following the Kolmogorov model, can be calculated using the subsequent expression [57]:

$$\sigma_{I,pt}^2 = \exp \left( \frac{0.49\sigma_R^2}{\left(1 + 1.11\sigma_R^{\frac{12}{5}}\right)^{\frac{7}{6}}} \frac{0.51\sigma_R^2}{\left(1 + 0.69\sigma_R^{\frac{12}{5}}\right)^{\frac{5}{6}}} \right) - 1, \tag{7}$$

where  $\sigma_R$  is the Rytov index, which, when considering the OGS's height, can be calculated as follows [53,57]:

$$\sigma_R^2 = 2.25k^{\frac{7}{6}} \sec^{\frac{11}{6}}(\zeta) \int_{H_{GS}}^{H_{Turb}} C_n^2(h)(h - H_{GS})^{\frac{5}{6}} dh. \tag{8}$$

Finally, the loss (dB) induced by turbulence for a given outage probability  $p_0$  is calculated according to the Kolmogorov model by including the aperture averaging effect as follows [58]:

$$L_{sci} = 4.343 \times \left[ \operatorname{erf}^{-1}(2p_0 - 1) \cdot \left[ 2\ln(\sigma_I^2 + 1) \right]^{\frac{1}{2}} - \frac{1}{2}\ln(\sigma_I^2 + 1) \right]. \tag{9}$$

### 3.2.5. Night-Time Sky Radiance and Urban Background Noise

In FSO-QKD, much like in traditional communication methods, the effectiveness of a link is largely determined by the SNR. While conventional communication techniques can enhance SNR by boosting the signal strength, QKD operates differently since it relies on utilizing a single-photonic qubit to transmit information. Consequently, reducing noise becomes the sole strategy for enhancing SNR in QKD systems. The SNR, in this context, is quantified by comparing the average number of photons that carry the signal to the noise photons detected per pulse by the SNSPDs/SPADs. The primary sources of noise in these systems are dark counts and ambient light contribution. Dark counts, which are false counts by the detector in the absence of actual signal photons, can be minimized in SPADs to rates fewer than 25 Hz by operating them at the Geiger mode. Meanwhile, for SNSPDs, the dark count rate (DCR) can be reduced to values that are as low as the mHz scale [59]. However, in free-space paths, such as those used in satellite-to-ground QKD, the system is vulnerable to background radiation, which significantly contributes to noise [60]. Background radiation comes from natural sources like the sun, moon, and stars, whose light can be scattered by atmospheric elements such as molecules, aerosols, fog, and clouds, thereby increasing background noise. Although human-made light, like city illumination, also adds to the background noise, its impact can be minimized by strategically locating the OGS away from urban areas. In this work, we primarily addressed natural background light as a noise source during night-time (new moon) conditions, whereas in ref. [37], the background noise that was generated within urban areas, as well as daylight QKD, was discussed. The consideration of daytime conditions poses challenges due to the difficulty in mitigating the noise resulting from excessive solar radiance, and it is considered out of the scope for the present work. The background radiance that reaches the detectors can be provided by the following equation:

$$P_{back} = H_{rad} \times \Omega_{FOV} \times A_r \times \Delta\lambda, \tag{10}$$

where  $H_{rad}$  ( $W/m^2sr \mu m$ ) represents the energy density of the background radiance, which originates both from the night sky radiance and the artificial urban radiance. The field of view of the receiver's aperture is denoted by  $\Omega_{FOV}$  (sr), while the receiver's capture area is given by  $A_r$  ( $m^2$ ), and the width of the receiver's band-pass optical filter is represented by  $\Delta\lambda$  ( $\mu m$ ).

### 3.2.6. Fiber Coupling Efficiency

In addition to the factors affecting the channel efficiency that were discussed previously, this study also explored the influence of turbulence on the spatial coherence of the beam. The latter directly affects the beam’s ability to be coupled with an SMF, a critical aspect when employing fiber-based detectors at the receiver’s side for DV- and ENT-based QKD. AO systems present a viable approach to mitigate the perturbations caused by a free-space channel [61]. By compensating for phase fluctuations due to atmospheric turbulence in real time, AO systems are not only pivotal in ground-based astronomy [62], but they are also emerging as essential for free-space optical telecommunications [61,63] and free-space QKD [63–65].

While existing studies have examined the uplink scenario to some extent [66,67], most of the research on space–ground QKD has focused on the downlink channel. As mentioned before, our investigation also addresses the downlink configuration. We modeled the fiber coupling efficiency of a QKD downlink by expressing the coupling efficiency  $\eta_{FC}$  through Strehl ratio-like metrics, since the latter has been suggested as an estimator for SMF coupling efficiency [68]. We also took into account the optical coupling efficiency  $\eta_0$ , which reflects the mismatch between an unperturbed received optical beam and the Mode Field Diameter (MFD) of the SMF. Although our model may not perfectly represent a true SMF coupling, it provides a solid approximation of fiber coupling efficiency. A more-detailed analytical model of SMF coupling, including detailed AO modeling, can be found in the literature [38,69,70].

In detail, the Strehl ratio (SR) in the presence of atmospheric turbulence is given as follows [53]:

$$SR = \left[ 1 + \gamma \left( \frac{D_r}{r_0} \right)^{5/3} \right]^{-6/5}, \tag{11}$$

where factor  $\gamma$  accounts for the level of AO correction and can take the values 1, 0.28, and 0 for no correction, tip tilt correction, and full-AO correction, respectively; whereas  $r_0$  is the Fried parameter that characterizes the atmospheric turbulence across the slant path, which is given by the following equation:

$$r_0 = \left[ 0.42 k^2 \sec(\zeta) \int_{H_{GS}}^{H_{Turb}} C_n^2(h) dh \right]^{-3/5}. \tag{12}$$

It is important to note that only perfect correction was considered here, meaning that, for example, the tip–tilt correction ( $\gamma = 0.28$ ) completely removes any second-order distortion to the wavefront, while a full-AO correction ( $\gamma = 0$ ) removes all the aberrations, thus resulting in a diffraction limited spot. In accounting for the efficiency of the receiving telescope, we also modeled the optical coupling efficiency, which was determined by the design optics of the receiving telescope [35]. The ideal coupling efficiency can be parametrized by the following:

$$\eta_0 = 2 \left[ \frac{\exp(-\beta^2) - \exp(-\beta^2 a^2)}{\beta \sqrt{1 - a^2}} \right]^2, \tag{13}$$

where  $a$  and  $\beta$  are given by

$$a = \frac{D_{obs}}{D_r}, \quad \beta = \pi \frac{D_r}{4\lambda} \frac{MFD}{f}, \tag{14}$$

where  $D_{obs}$  is the obscuration aperture diameter;  $MFD$  denotes the mode–field–diameter of an SMF fiber, which is equal to 10.4  $\mu\text{m}$ ; and  $f$  is the focal length of the receiving telescope. Since the mode characteristic of an SMF can be represented by a Gaussian function, and as it is given that the aperture plane and the focal plane are interconnected through a Fourier transform [71], optimal coupling is possible only when a Gaussian beam matches the aperture within the coupling optics. Nevertheless, the average profile of incoming

light tends to exhibit a flat-top distribution [72], which sets a theoretical upper limit to the coupling efficiency of approximately 81% when assuming a non-turbulent transmission, which can be extracted from Equation (13) for  $\alpha = 0$  and  $\beta = 1.12$ . Finally,  $\eta_{sys}$  accounts for the AO/tip-tilt system optical components' transmittance. The estimated coupling efficiency can then be determined by

$$\eta_{FC} = \eta_{sys}\eta_0SR. \tag{15}$$

At this point, it is important to note that multi-mode fiber (MMF) coupling could be employed instead of SMF coupling to enhance the coupling efficiency. However, in this study, we focused on SMF coupling as it is more widely used in long-distance telecom photon distribution due to its lower degree of loss. A comparison between MMF and SMF coupling could be valuable, but the model is fundamentally different for a MMF and is beyond the scope of the current work. Therefore, we have not included MMF coupling in our analysis.

### 3.3. Protocol Assumptions and Finite Key Size Analysis

Since the atmospheric polarization decoherence of the atmosphere has been measured as being limited [73], polarization-based QKD protocols appear to be suitable for satellite-to-ground QKD communication. For this reason, the efficient Decoy-State BB84 (DS-BB84) protocol, which employs the “weak + vacuum” configuration detailed in [74], was selected. The protocol integrates decoy and vacuum states into the traditional BB84 framework to mitigate the Photon Number Splitting (PNS) attacks. This incorporation enables precise assessments of background noise and channel loss, enhancing the protocol's ability to detect eavesdropping attempts. Consequently, the decoy state protocol exhibits decreased susceptibility to PNS attacks, thus allowing for higher mean photon numbers per pulse.

The finite key size effect was considered for the protocol modeling. Finite key size in QKD refers to the limited number of secret key bits that can be extracted from the quantum signals exchanged between communicating parties. It is a critical consideration in QKD protocols because a finite key size directly affects the security of the shared key. With a limited number of key bits, the statistical fluctuations between ones and zeros should be considered as these result in disruptions of the key homogeneity, which increase information leakage or induce key compromises through specific attacks (such as collective attacks) [75,76]. Therefore, accounting for finite key size is essential to accurately assess the security level of the key generated through QKD, as well as to implement appropriate error correction and privacy amplification techniques to mitigate the effects of finite-size effects and ensure the integrity of the secret key.

When considering a finite post processing block size, the statistical fluctuations of the visibility were included.  $Q_\mu$  corresponds to the gain of the signal state and  $E_\mu$  corresponds to the overall QBER. The values of  $Q_\mu$  and  $E_\mu$  can be calculated as

$$Q_\mu = Y_0 + \exp(-\eta\mu), \tag{16}$$

$$E_\mu = \frac{e_0Y_0 + e_{sys}(1 - \exp(-\eta\mu))}{Q_\mu}, \tag{17}$$

where  $\eta$  corresponds to the overall link transmittance;  $e_{sys}$  corresponds to the baseline system error rate and is equal to  $(1 - V)/2$  (where  $V$  corresponds to the total polarization visibility of the Bob station, i.e., the limited Polarization Extinction Ratio (PER) of the Bob's polarization analysis module, as well the polarization error due to polarization basis deviation);  $e_0$  corresponds to the error rate of the background noise;  $e_0$  is set to  $1/2$  by assuming that the background noise is random; and  $Y_0$  corresponds to the probability of the detector to click due to dark counts, background noise, or due to after pulsing probability (for the case of SPAD detection). The latter is expressed as follows:

$$Y_0 = P_{dc} + P_{back} + P_{ap}. \tag{18}$$

$P_{back}$  can be calculated according to the background radiance value as follows:

$$P_{back} = t_{gate} \eta_{Rx} \eta_{FC} \frac{P_{back}}{h \cdot f}, \tag{19}$$

where  $h \cdot f$  correspond to the single-photon energy;  $t_{gate}$  to the effective detection time window;  $\eta_{Rx}$  and  $\eta_{FC}$  to the receiver system (filter loss, polarization controller loss, etc.), and fiber coupling overall efficiencies, respectively; and  $P_{back}$  to the receiver background solar radiance, which is provided by Equation (19).

For the calculation of the SKR, we assumed security against restricted collective attacks and followed the methodology reported in [75,76].

$$SKR \geq f_{rep} \times q \left\{ Q_1 [1 - H_2(e_1)] - Q_\mu f(E_\mu) H_2(E_\mu) - \frac{\Delta}{N_s} \right\} \eta_{dead}, \tag{20}$$

where  $\eta_{dead}$  corresponds to the dead time efficiency, which accounts for the limitations in maximum count rates due to the detectors' dead time [77];  $f(E_\mu)$  is the non-ideal error correction efficiency; and  $N_s$  is the total number of transmitted signal states. The value of  $\Delta$  was calculated to be the following [75]:

$$\Delta = 7 \times \sqrt{N_n \times \log_2 \left( \frac{2}{\epsilon_s - \epsilon_{pe}} \right)} + 2 \times \log_2 \left( \frac{1}{2 \times (\epsilon - \epsilon_s - \epsilon_{ec})} \right), \tag{21}$$

where  $\epsilon_s$  corresponds to the smoothing parameter,  $\epsilon_{pe}$  to the estimation parameter, and  $\epsilon_{ec}$  to the error correction parameter, while  $\epsilon$  denotes the overall security parameter of the final key, which is the sum of the aforementioned parameters. The finite key size effects also play a vital role in satellite-based QKD since the communication time windows during which the satellite is visible by an OGS vary for different orbits and remain limited for specific cases.

#### 4. Simulation Results

In this section, the simulated results are presented and discussed. A single satellite pass was set as the baseline, while the key rates were compared for each different scenario. Initially, the requirements for operational satellite-to-ground QKD are discussed; subsequently, the effect of the key parameters, such as fiber coupling and receiver telescope aperture size, on the link's performance is studied, which is achieved by following the distribution of a single photon over terrestrial fiber links. For the analysis presented below, the system parameters were kept constant while others were placed between some other range of different values. The input parameters are included in Table 1 below.

**Table 1.** System assumptions and parameters.

Symbol	Parameter	Value
$\lambda$	Quantum channel wavelength	1550 nm
$f$	Emission rate	40–300 MHz
$N_t$	Transmitted block size	$10^{10}$ – $10^{13}$ bits
$H_{sat}$	Satellite orbit altitude	550/8000/36,000 km
$D_{Tx}$	Tx telescope aperture diameter	0.3 m
$D_{Rx}$	Rx telescope aperture diameter	0.28–2.3 m
$a$	Obscuration ratio	~0.1
$f/x$	Focal ratio	~ $f/8$
$\eta_{sys}$	AO/tip–tilt optical transmittance	0.9
$H_{OGS}$	OGS Altitude	500–2340 m
$\epsilon$	Min. elevation angle	20°
$\sigma_p$	Pointing error variance	0.7 $\mu$ rad

Table 1. Cont.

Symbol	Parameter	Value
$\eta_{Bob}$	Detector’s setup loss	2 dB
$C_n^2$	Refractive index structure parameter	$1.7 \times 10^{-14} - 1.7 \times 10^{-13} \text{ m}^{-2/3}$
$H_{rad}$	Background solar radiance	$1.5 \times 10^{-5} - 1.5 \times 10^{-1} \text{ W/m}^2\text{sr } \mu\text{m}$
$p_0$	Outage probability	1%
$\Omega_{FOV}$	Receiver’s FOV	100 $\mu\text{rad}$
$\lambda_{pass}$	Filter’s spectral passband	0.2 nm
$\eta_{filter}$	Filters efficiency	0.7
$\mu$	Mean signal photon/pulse	0.7
$\nu$	Mean decoy photon/pulse	0.1
$\epsilon_s$	Smoothing parameter	$9 \times 10^{-11}$
$\epsilon_{pe}$	Parameter estimation	$7.7 \times 10^{-11}$
$\epsilon_{ec}$	Error correction parameter	$8 \times 10^{-11}$
$\eta_{SNSPD}$	SNSPDs detection efficiency	0.85
$DCR_{SNSPD}$	SNSPDs dark count rate	10 cps
$\tau_{dead\_SNSPD}$	Dead time SNSPD	30 ns
$\eta_{SPAD}$	SPADs detection efficiency	0.15
$DCR_{SPAD}$	SPADs dark count rate	300 cps
$\tau_{dead\_SPAD}$	Dead time SPAD	20 $\mu\text{s}$
$t_{gate}$	Effective gate time window	1 ns
$e_0$	Error probability for noise counts	50%

#### 4.1. Source Specification/Requirement Analysis

Due to the constraints in satellite QKD communications, such as the signal loss that takes place in free-space transmission due to turbulence-induced phenomena, as well as the limited time window for satellite visibility, the number of single photons that can be securely exchanged between two parties are limited. This limitation affects the efficiency of privacy amplification and error correction processes, which are crucial for ensuring the security and integrity of the keys. In space-based QKD, where satellites are used to distribute keys between ground stations over vast distances, the finite key size imposes additional challenges [41].

In the following sub-section, the effect of the finite key size effect in various orbits is studied. As described above, a specific block size is used for the secure key distillation. Small block sizes are unable to provide secure key distillation when accounting for the finite key size effects, and since different orbits provide different communication time windows and link budgets, different systems requirements should be considered. For this sub-section, only tip-tilt correction was assumed for the cases in which fiber coupling was considered. In what follows, the minimum requirements for enabling key distillation over a single satellite pass in LEO, MEO, and GEO orbits in terms of Alice’s emission rate and iQBER are examined.

##### 4.1.1. Emission Rate Analysis—LEO

To begin with, a LEO satellite pass was simulated. For simplicity, we will assume an ideal LEO pass over the Helmos OGS in Greece (Latt: 37.98, Long: 22.20), meaning that the satellite reaches a maximum elevation angle of 90 degrees. For this ideal case, the satellite was visible (>20° elevation) for approximately 5 min and 30 s. For this first case study, a ground station at 500 m was simulated. In addition, a 1 m aperture telescope, with a 0.08 m secondary mirror and a 10 m focal length, was assumed for the receiver station. Figure 3 provides the end-to-end link loss (Y-right axis), as well as the expected normalized SKR (bps/pulse) (Y-left axis) over time, where different transmitted block sizes values were assumed. Mere tip-tilt correction was considered for the telescope-to-SMF coupling (corresponding to a value of  $\gamma = 0.28$  in Equation (15)) while considering both (a) SNSPD and (b) SPAD detectors. Since the link loss was higher when SPADs were used as detection units, higher transmitted block sizes were required. Since future OGSs might



be equipped with either detector type, a sufficient transmitted block size that can comply with these two detection systems seems to be about  $N_{trans} > 10^{10}$  bits. To achieve this, the on-board source was required to provide an emission rate of approximately  $f_{rep} > 40$  MHz, which is compatible with the typical achievable detection rates of both SPAD and SNSPD detectors. Considering the normalized calculated SKRs, as well as by assuming an emission rate of 40 MHz (which yields a maximum transmitted block size of  $10^{10}$  bits in the case of LEO, i.e., where the satellite is only visible for 300 s), an average SKR of 8 kbps and 800 bps were calculated for the case of SNSPD and SPAD detection, respectively, over a single LEO passage. It is important to note that, once again, the calculations above provide the minimum requirements for key distillation. These results can be enhanced if one considers state-of-the-art sources that can provide higher transmitted block sizes, larger receiver apertures, or a full-AO correction of the turbulent wavefront. The aforementioned parameters will be discussed in Section 5.

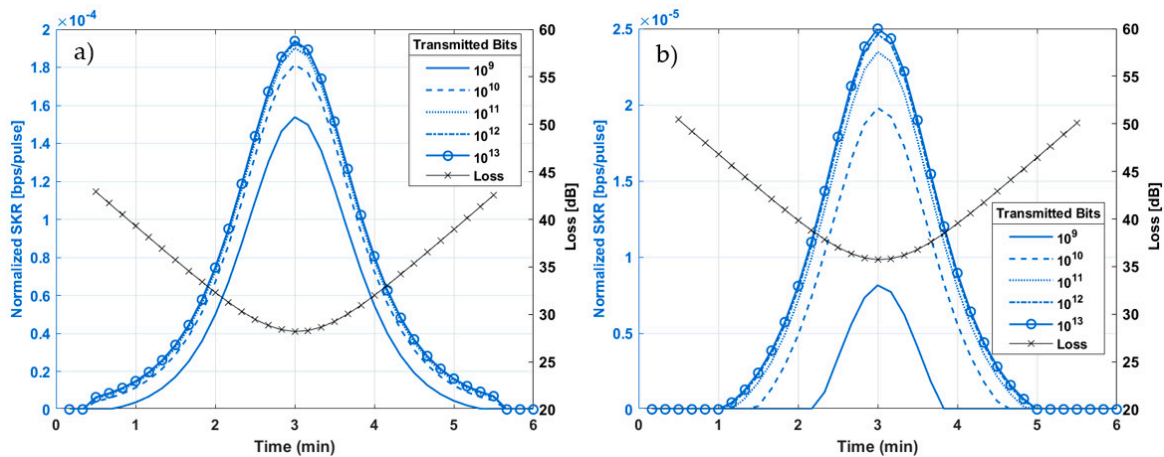


**Figure 3.** End-to-end link loss over time, as well as the expected normalized SKR over time for different transmitted block sizes values, in telescope-to-SMF coupling, all while considering both (a) SNSPD detectors and (b) SPAD detectors.

#### 4.1.2. Emission Rate Analysis—MEO

Next, a MEO satellite pass was considered for the emission rate requirement analysis. For the purposes of our analysis, the O3b MEO orbit was simulated; therefore, the constellation was considered as flying across the equator. Additionally, the OGS location had to be specified for the calculation of the satellite’s elevation angle over time. Therefore, the Helmos OGS (Latt: 37.98, Long: 22.20) location in Greece was selected for the simulation of the MEO satellite pass. It should be noted here that for OGSs with a higher latitude the maximum achievable elevation angle will be lower. For an MEO satellite and the Helmos OGS, the maximum achievable elevation angle was calculated to be just above 30 degrees. Figure 4 once again presents the end-to-end link loss alongside the projected normalized SKR over time. This analysis assumes a range of transmitted block sizes and incorporates tip–tilt correction under three distinct scenarios: (a) a scenario featuring a receiver aperture of 1 m and SNSPDs coupled with the telescope to the SMF, (b) a scenario with a 1.5 m receiver aperture also using SNSPDs and telescope-to-SMF coupling, and (c) a scenario involving a 2.3 m receiver aperture with free-space SPAD detection. That time, it was evident that, as shown in Figure 4, transmitted block sizes of  $N_{trans} > 10^{12}$  bits were required to provide adequate post projecting block sizes for all three scenarios. Given the above—as well as when considering that, then, the satellite was visible for a time window of more than 50 min—the required emission rate of the on-board source was calculated to be in the order of a few hundreds of MHz (ca. 300 MHz).

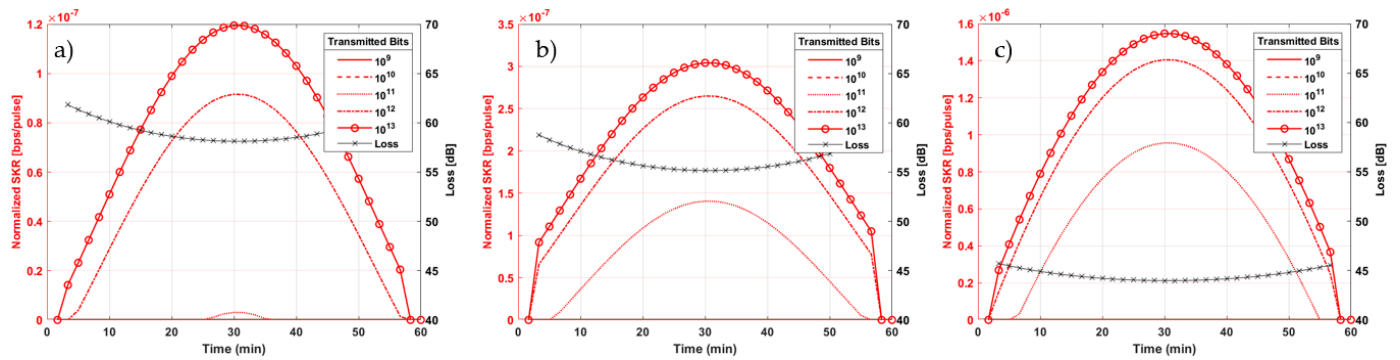


**Figure 4.** End-to-end link loss and normalized SKR over time for different transmitted block size values of (a)  $D_{rx} = 1$  m and SNSPD with SMF coupling, (b)  $D_{rx} = 1.5$  m and SNSPD with SMF coupling and (c)  $D_{rx} = 2.3$  m and SPAD without SMF coupling.

Considering the above, for the three distinct scenarios, the average SKRs of  $\sim 30$  bps,  $\sim 75$  bps, and  $\sim 420$  bps were, respectively, calculated. The best performance took place when seemingly very large telescope apertures (2.3 m) were employed and combined with a free-space SPAD detection that can bypass the limited telescope-to-SMF coupling efficiency tip-tilt correction provides. However, large apertures ( $>1.9$  m) were found to be necessary for SPADs to support MEO-to-ground QKD, and this only worked when assuming free-space detection. Despite this, it is not clear whether SPAD detection is able to support repetition rates as high as 300 MHz due to the electronic limitations of the devices, such as having a high jitter. On the other hand, SNSPDs can provide low jitter, but they usually require fiber coupling. Nonetheless, MEO orbits can be feasible for QKD under certain assumptions, such as receiver aperture or OGS latitude, thus providing much longer time windows, yet limited SKRs.

#### 4.1.3. Emission Rate Analysis—GEO

Finally, GEO orbit requirements in terms of emission rates were discussed. GEO satellites provide a continuous time window and a fixed elevation angle, but the elevation angle is based on the OGS position, as in the case of MEO satellites. For this study, an elevation angle of 45 degrees was considered, which is a typical elevation angle for the corresponding GEO satellite providers of Greece. The communication time window was limited to 12 h since only night-time communication was considered. As before, Figure 5 provides, again, the end-to-end link loss over time, as well as the expected normalized SKR over time, where different transmitted block sizes values for the following three different scenarios were assumed: (a) a receiver aperture of 1.5 m and SNSPD detection with telescope-to-SMF coupling, (b) a receiver aperture of 2.3 m and SNSPD detection with telescope-to-SMF coupling, and (c) a receiver aperture of 2.3 m and free-space SNSPD detection. Free-space SNSPD detection has been presented within the literature [78,79], but often with limited detection efficiency. In this case, we assumed that the detectors were capable of detecting photons via free space without limiting their efficiency. Considering the link budget for the scenarios above, as well as the time communication windows for GEO satellites, an emission rate of  $\sim 200$  MHz was required for the space source to provide a transmitted block size of  $N_{trans} = 10^{13}$  bits over 12 h.

It was calculated that, for the first two assumptions (as shown in Figure 5a,b), SKRs of less than 10 bps were calculated, whereas (as shown in Figure 5c), SKRs of up to 320 bps for the third case may be achieved. Despite this, it is yet unclear to which extent free-space SNSPDs can function without severely limiting the system efficiency and not drastically increasing the ambient background noise. Therefore, considering the very low SKR, which was provided via fiber-coupled SNSPDs, it seems that large astronomical telescopes must be used over long periods to provide the necessary key volumes to be able to distill secure keys after hours of communication. If including the possibility of cloud coverage within

the night, as well as an increase in the background noise (e.g., due to the moon’s presence), then the GEO-to-ground QKD will be interrupted. Therefore, we conclude that, under these assumptions, GEO-to-ground QKD communication does not seem like a viable alternative compared to LEO and MEO orbits. As such, under the selfsame aforementioned assumptions, they will thus be excluded from now on in our results. Further insights on how GEO orbit may benefit QKD communication will be discussed in Section 5.

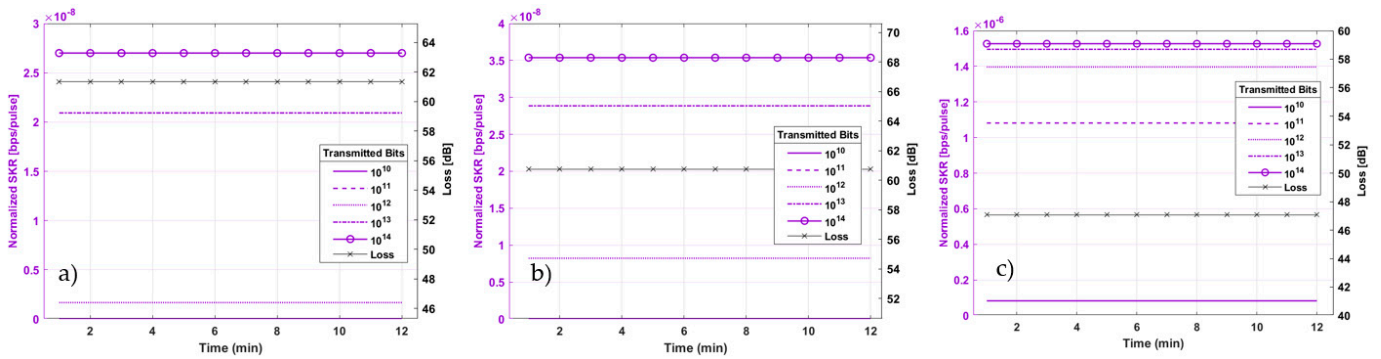


**Figure 5.** End-to-end link loss and normalized SKR over time for different transmitted block size values of (a)  $D_{rx} = 1.5$  m and SNSPD with SMF coupling, (b)  $D_{rx} = 2.3$  m and SNSPD with SMF coupling, and (c)  $D_{rx} = 2.3$  m and SNSPDs without SMF coupling.

#### 4.2. iQBER Analysis

##### 4.2.1. iQBER Analysis—LEO

A critical factor influencing both the performance and security of space-based QKD systems is the intrinsic QBER (iQBER) of the space-based sources. The iQBER is essentially a measure of the error rate of the erroneous quantum bits transmitted by the source, and it directly impacts the fidelity and trustworthiness of the quantum communication channel. In the context of space-based QKD, where the communication link spans hundreds to thousands of kilometers through the vacuum of space and the Earth’s atmosphere, even sources with seemingly low iQBER (1.5%) can significantly diminish the efficiency of key generation and the security of the transmitted keys. A higher iQBER necessitates more robust error correction and privacy amplification procedures to extract a secure key, which, in turn, reduces the effective key generation rate and increases the complexity and resource requirements of the QKD protocol. Therefore, minimizing the iQBER of a space-based QKD source is paramount for optimizing the system’s performance.

Figure 6 presents the calculated SKR for a single satellite pass assuming various source’s iQBER values for (a) SNSPD detection with SMF coupling, (b) SPAD detection with SMF coupling, and (c) free-space SPAD detection. For these results, a receiver aperture diameter of 1 m was assumed along with a transmitted block size of  $10^{10}$  bits and a mere tip–tilt correction. It is evident that even a value of 1% for the intrinsic QBER can have an effect of up to 20% lower SKR values compared to the ideal case. Furthermore, it was observed that higher values of iQBER do not drastically affect the key rates but can limit the communication time window for cases where the overall end-to-end loss is high (e.g., SPAD detection with SMF coupling (Figure 6b)). To enable the satellite segment to accommodate flexible OGS, which may be equipped with either SPADs or SNSPDs, an iQBER value of less than 2% is recommended under our assumptions. Performance analysis for a LEO case using state-of-the-art GHz-scale sources [29,30] with an iQBER below 1% will be discussed in Section 5.

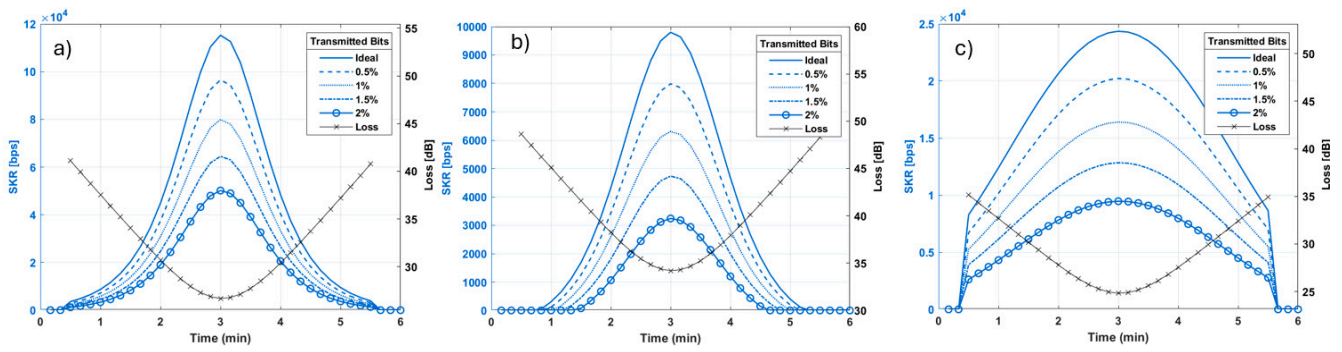


**Figure 6.** End-to-end link loss and normalized SKR over time for the different i-QBER values of (a)  $D_{rx} = 1$  m and SNSPD with SMF coupling, (b)  $D_{rx} = 1$  m and SPAD with SMF coupling, and (c)  $D_{rx} = 1$  m and SPAD without SMF coupling.

#### 4.2.2. iQBER Analysis—MEO

In this section, we vary the iQBER of the MEO-source to conduct a feasibility analysis by leveraging the requirements for the on-board source emission rate (250 MHz) and transmitted block size ( $10^{12}$  bits) that are derived from Section 4.1.1. For a single MEO satellite pass, when assuming a receiver aperture diameter of 1 m, the only scenario that yields non-zero key rates under the assumption of tip-tilt correction is when the SNSPDs are employed as detection units. Figure 7 presents the expected SKR values over time assuming different iQBER values. It has been observed that MEO satellites can grant QKD links with imperfect sources if SNSPDs are employed in the detection setup for long time windows. On the other hand, the maximum achieved rates were about four orders of magnitude lower compared with the LEO orbit under the same detection assumptions. To enhance the performance in the MEO case, where the source’s iQBER is high, improvements in the overall link budget should be considered, such as selecting a bigger receiver aperture, AO correction, or a GHz-scale source.

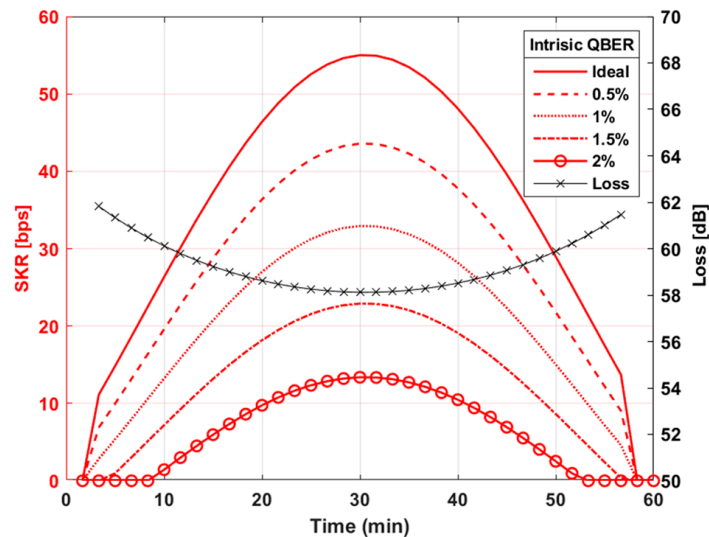


**Figure 7.** End-to-end link loss and normalized SKR over time for  $D_{rx} = 1$  m and SNSPD with SMF coupling.

#### 4.3. Noise Tolerance Analysis

Until this point, the background noise radiance had been set to a constant value that corresponded to limited noise contribution. In this sub-section, we shall discuss the effect of the background noise in the key rates when assuming different satellite orbits. Since our analysis takes into consideration only night-time conditions, we varied the background



noise radiance to correspond to four distinct scenarios, namely clear night, new moon, full moon, and urban night.

#### 4.3.1. Noise Tolerance—LEO

To begin with, the effect of background noise in LEO-to-ground QKD links is discussed. Various night-time radiance conditions are being considered according to [33], and they correspond to different radiance values, which are mainly dependent on the moon’s cycle. Once again, an emission rate of 250 MHz and a transmitted block size of  $10^{10}$  bits were considered. Figure 8 presents the distilled key bits over time for a single satellite pass, and this was achieved by considering different sky radiance values for (a)  $D_r = 1$  m and SMF-coupled SNSPD detection, (b)  $D_r = 1$  m and SMF-coupled SPAD detection, and (c)  $D_r = 1$  m and free-space SPAD detection. It is evident that fiber coupling renders the system much more robust to background noise as it enables QKD communication even under full moon, night-time conditions. For the case of SNSPD detection, since the SNR is improved due to the higher quantum efficiency granted by the detectors, the system can also (barely) perform under daytime conditions ( $H_{rad} = 1.5 \text{ W/m}^2\text{sr } \mu\text{m}$ ), yet only with extremely limited communication time windows.

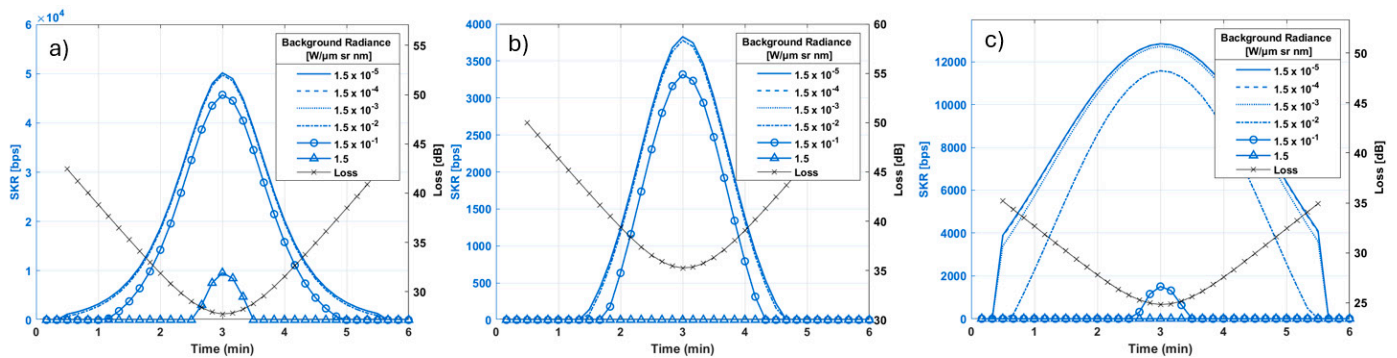


**Figure 8.** SKR over time for a single satellite pass when varying the sky radiance values of (a)  $D_r = 1$  m and SMF-coupled SNSPD detection, (b)  $D_r = 1$  m and SMF-coupled SPAD detection, and (c)  $D_r = 1$  m and free-space SPAD detection.

Additionally, despite the lower overall link budget, the SPADs also seemed to be robust in terms of sky radiance when fiber coupling was considered, and this was without being severely disturbed by the moon’s presence. On the other hand, free-space-coupled SPAD systems are much more vulnerable to background noise, yet they perform with higher key rates due to the lack of the lossy SMF coupling during different night-time conditions.

#### 4.3.2. Noise Tolerance—MEO

The effect of background noise in QKD links is strongly dependent on the links with overall efficiency; therefore, we shall expect a great influence on the noise in the achieved key rates for MEO-to-ground QKD links, where end-to-end loss is much higher. Figure 9 presents the distilled SKR over a single MEO satellite pass when considering different sky radiance values for (a)  $D_r = 1$  m and (b)  $D_r = 2.3$  m, of which both had SMF-coupled SNSPD detection. As discussed before, in the MEO-QKD case, the source’s iQBER was set to 1.5%, whereas the overall number of transmitted bits was set to  $10^{12}$  bits. It was observed that MEO-to-ground QKD links are indeed very unstable in terms of variations in the sky radiance. Since the end-to-end loss was already relatively close to the key distillation limits, variations in the background noise were able to completely interrupt the QKD communication. It was evident that, as shown in Figure 9b, even with a much bigger receiver with a 2.3 m aperture diameter, key exchange was only possible under clear night and new moon conditions. In conclusion, this limitation would severely affect the availability of MEO satellites for delivering keys to the ground segment. To tackle this, a combination of narrower filters along with shorter detection time windows may



allow for the MEO QKD communication to become feasible for increased background solar radiance values.

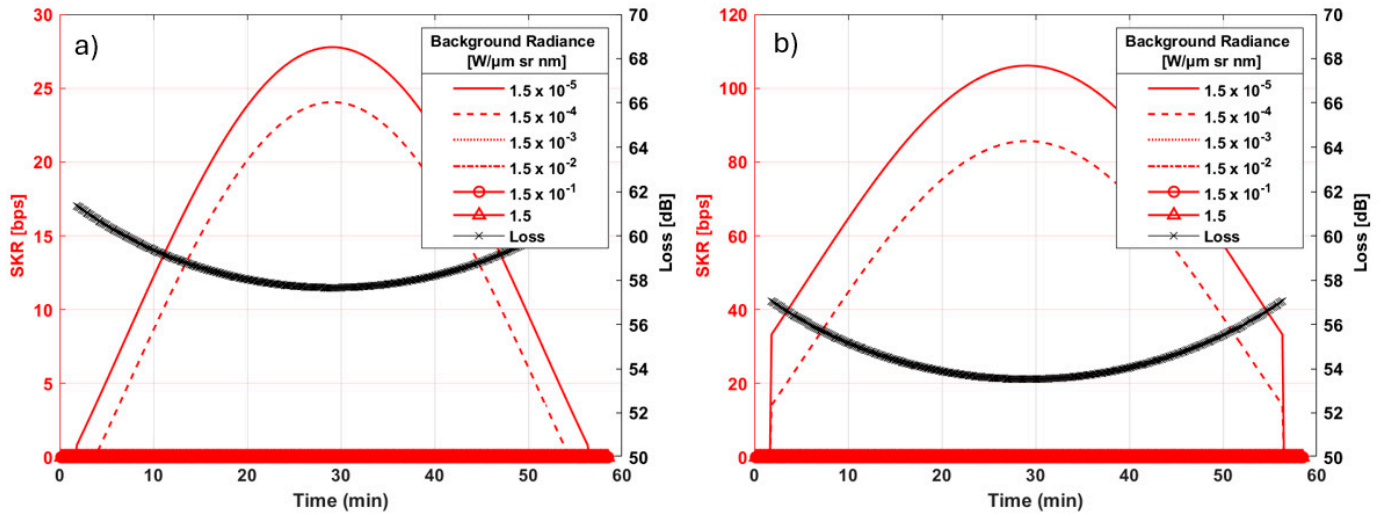
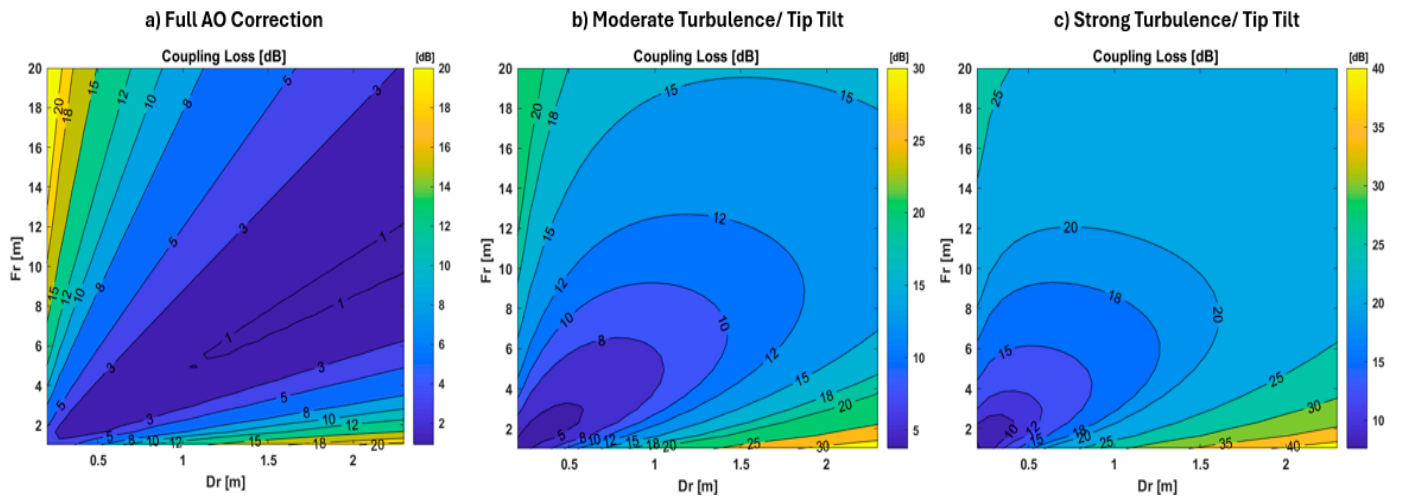


**Figure 9.** SKRs over a single MEO satellite pass when varying the sky radiance values of (a)  $D_r = 1$  m and SMF-coupled SNSPD detection and (b)  $D_r = 2.3$  m and SMF-coupled SNSPD detection.

#### 4.4. Receiver Size and Design Characteristics

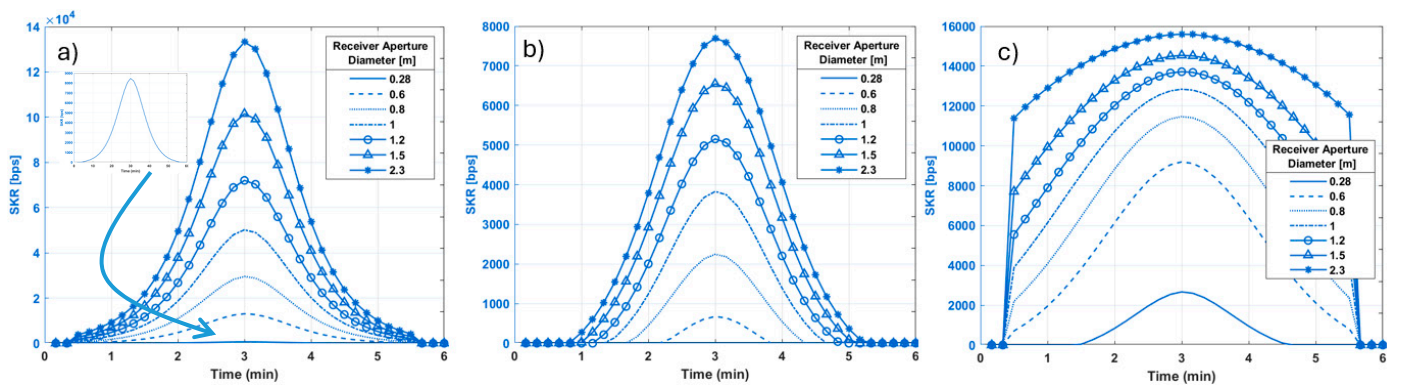
Addressing the technical challenge of coupling an optical satellite signal into a ground receiver involves overcoming unique obstacles compared to traditional Radio Frequency (RF) communications. Optical satellite communications encounter several challenges due to the nature of light propagation and atmospheric conditions. Coupling from free space to SMF, particularly for large telescopes, presents significant challenges in the presence of turbulence as it requires matching between the incoming beam’s intensity distribution and phase front [62]. To address this issue, AO systems were utilized, leading to a notable improvement in fiber coupling efficiency. These systems enable coupling efficiencies over 50%, even in the case of large telescopes. The upcoming section delves into how different system parameters, such as the telescope’s focal length and aperture diameter, influence the overall efficiency of fiber coupling. Furthermore, it explores the viability of satellite QKD across a range of receiver telescope aperture sizes. It is important to highlight that, for each aperture size considered, a corresponding focal length was chosen to optimize fiber coupling. This focal length was determined to be ten times the value of the aperture diameter, thus ensuring that the fiber coupling capabilities are not compromised by a fixed focal length across different telescope sizes. Additionally, each telescope was assigned an obscuration ratio of 0.1, thus further tailoring the setup to maximize coupling efficiency. Incorporating the top-down approach outlined earlier, our focus here was solely on the LEO case. An in-depth discussion on how the characteristics of the receiver impact MEO and GEO cases will be addressed in Section 5.

Figure 10 depicts a contour plot demonstrating the coupling efficiency  $\eta_{FC}$  of the SMF, computed using Equation (12), with respect to the receiver’s telescope  $F_r$  (m) and aperture diameter  $D_r$  (m) under the conditions of full-AO and tip-tilt correction amidst moderate ( $C_n^2 = 10^{-14} \text{m}^{-2/3}$ ) and strong turbulence ( $C_n^2 = 10^{-13} \text{m}^{-2/3}$ ). The calculation assumed a satellite elevation angle of 90 degrees, with the receiver situated at an altitude of 500 m. To incorporate the direct impact of atmospheric turbulence, Equation (15) was employed. Specifically, the  $\gamma$  in Equation (11) was set to 0 for full-AO correction, while it took values of 0.28 and 1 for the tip-tilt correction and no correction, respectively. The telescope’s efficiency was factored in using Equation (14), where  $D_{obs}$  remains constant at 0.1.



**Figure 10.** Contour plots of the SMF coupling loss (dB) over focal length  $F_r$  and receiver aperture diameter  $D_r$  for (a) full-AO correction, (b) tip-tilt correction for  $C_n^2 = 10^{-14} \text{ m}^{-2/3}$ , and (c) tip-tilt correction for  $C_n^2 = 10^{-13} \text{ m}^{-2/3}$  with an elevation angle of  $90^\circ$ .

Figure 11 depicts the calculated SKR over a single pass for (a) SNSPD detection with fiber coupling, (b) SPAD detection with fiber coupling, and (c) free-space SPAD detection. The calculation support in the case of SNSPD detection for telescopes with apertures as small as 0.28 m can support satellite QKD communications with a limited communication time window. Yet, SKRs reaching the order of hundreds of bits per second in average can be achieved. On the other hand, SPAD detection can support fiber coupling only with receiver telescope apertures larger than 0.8 m. On the contrary, for free-space SPAD detection, where the end-to-end loss remains limited, small-sized telescopes (e.g., a 0.28 m aperture) can support satellite QKD, thereby reaching maximum SKR values of up to 2 kbps. It was also evident that, as shown in Figure 11c, due to the dead time effect (note that  $t_{dead} = 20 \mu\text{s}$  for our assumptions), if large apertures are employed, then the value of the calculated SKR is not drastically increased since the detectors come closer to the saturation limit as the receiver aperture increases. Additionally, since the effect of atmospheric turbulence in the coupling was not present, high SKR values could be achieved, even in low elevation angles. Therefore, it was suggested that free-space SPAD detectors, combined with small- or medium-sized telescope apertures, may be the most cost-effective and practical selection for use cases where the point-to-point link terminates at the telescope location. At this point, it is worth mentioning that tracking LEO satellites with large telescopes, such as those with 2.3 m apertures, poses significant challenges due to their weight and slower movement capabilities.



**Figure 11.** SKR over time for the different  $D_{rx}$  values of (a) SNSPD with SMF coupling, (b) SPAD with SMF coupling, and (c) SPAD without SMF coupling.

#### 4.5. Fiber Distribution

In the following sub-section, the fiber distribution extension is discussed. For this use case, it was assumed that the quantum signal was not detected in the OGS site, where it is captured by the telescope, but it was further transmitted via a low-loss SMF. To investigate whether the remaining link budget allows for fiber transmission, additional loss was added to the modeling, which was attributed to the fiber distribution segment. Figure 12 depicts the calculated SKR over a single pass for (a) a 1 m telescope receiver, (b) a 2.3 m telescope receiver equipped with SNSPDs, and (c) a 1 m telescope receiver with SPAD detection. The space-based source iQBER was once again set to 1.5%, while the number of transmitted bits was set to  $N_{trans} = 10^{10}$ . For the fiber coupling, tip-tilt correction was considered. As expected, larger apertures yield higher link budgets, enabling the transmission of collected single photons over larger fiber distances, without the need for a trusted node in the OGS position. It was evident that, as shown in Figure 12b, key rates of up to 1 kbps can be achieved when the satellite reaches the maximum elevation angles, with an additional 20 dB penalty attributed to the fiber segment (i.e., up to about 100 km of fiber distribution assuming an ideal fiber segment with no connection or bending losses). In general, for the three different assumptions of Figure 12, namely (a), (b), and (c), the key rates dropped to zero if the additional fiber loss exceeds 20 dB, 30 dB, and 7 dB, respectively. It is crucial to target a minimum value for the average required SKR on Bob’s side in order to determine the end-to-end link budget.

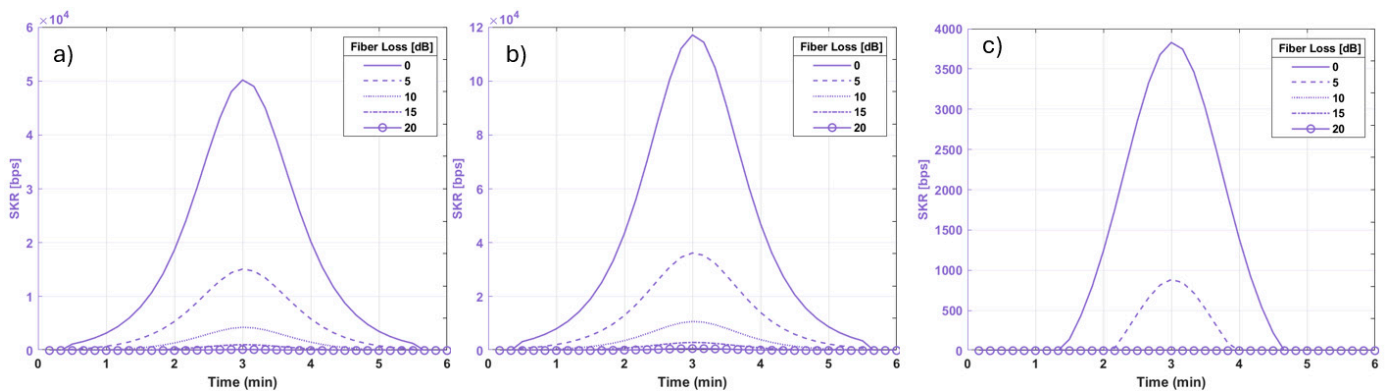


**Figure 12.** SKR over time accounting for the additional fiber distribution losses of (a)  $D_{rx} = 1$  m with SNSPD detection, (b)  $D_{rx} = 2.3$  m telescope receiver with SNSPD detection, and (c)  $D_{rx} = 1$  m telescope receiver with SPAD detection.

#### 5. Discussion

The analysis presented above met only the minimum requirements necessary to establish sufficient SKRs between a satellite and an OGS without incorporating any advanced equipment in either the space or ground segments.

Recent technological advances have significantly enhanced the performance of quantum sources and the capabilities of OGSs, including AO and SNSPDs. The subsequent section will explore a forward-looking approach, assuming the satellite is equipped with a GHz-scale source and uses the DS-BB84 protocol. The OGS is assumed to be ideally located, such as at the Helmos Observatory (which is situated at 2340 m above sea level), and the design features of the Helmos telescope were considered. Additionally, the link budget analysis considered the distribution of information beyond the OGS to assess the potential convergence of space and ground fiber segments using state-of-the-art equipment. For this use case, although the quantum signal was captured by the telescope at the OGS site, it was not detected there but was instead transmitted through a low-loss SMF (ca. 0.2 dB/km loss), as described in Section 4.5. The modeling included additional losses attributed to the fiber distribution segment to determine if the remaining link budget can support effective fiber transmission. More specifically, as shown in Figure 13, the calculated SKR for (a) single pass of a LEO satellite, (b) a single pass of a MEO satellite, and (c) a 12 h communication

between the OGS and a GEO satellite was depicted. To facilitate the comparison for the different fiber losses added, the  $y$ -axis was displayed on a semi-logarithmic scale. The updated assumptions for this case are listed in Table 2, while the parameters that are not included in Table 2 have remained unchanged and can be obtained from Table 1. Briefly, the 2.3 m Helmos telescope was considered as the receiver equipped with SNSPDs, whereas AO correction was also considered. Regarding the AO correction, we considered an almost perfect AO system ( $\gamma = 0.05$  in Equation (11)) capable of achieving an overall coupling efficiency of 36% (at an elevation angle of  $90^\circ$ ), in which an infinite control bandwidth was considered. For the case of AO, a more precise modeling would be needed, but that is beyond the scope of this work. As expected from the analysis conducted on Section 4, LEO orbits yield higher link budgets, thus enabling the transmission of qubits over greater fiber distances compared to MEO and GEO orbits. Figure 13a illustrates that, even with an additional 30 dB penalty due to fiber transmission, the achievable SKR can reach kbps for high elevation angles values. This 30 dB loss corresponds, ideally, to a fiber distance of 150 km. Such a distance typically exceeds the usual span of a single metropolitan area, often extending to a regional scale that could include multiple metropolitan areas or stretch from an urban center to rural or less densely populated regions. For the case of MEO and GEO that are presented in Figure 13b,c, respectively, the key rates dropped to zero when the additional fiber loss exceeded 15 dB for the case of MEO and 10 dB for the case of GEO. Nevertheless, the remaining link budgets of 15 dB and 10 dB ideally correspond to fiber distances of 75 km and 50 km, respectively, thus yielding tens of bps of SKRs. These distances typically fall within the range of a metropolitan area, enabling the information to be potentially distributed to urban centers and their surrounding suburbs. Since this section explores a more futurist approach, it might also be of interest to consider that, with the advent of novel low loss optical fibers [80], there will be telecom wavelengths with losses below 0.14 dB/km. With these advancements, the feasible distances for transmitting qubits may be significantly extended in the upcoming years, enabling the transmission of qubits from beyond LEO orbits to even longer distances.

To summarize our analysis, in Figure 14, we included all the orbits using, as a metric, the yearly distilled key bits achievable for each orbit, with the same assumptions. A figure of merit was provided, and bar plots of the annual distilled key bits available from each orbit were illustrated. Since, for LEO cases, the satellite is not always visible with the same elevation angle at each pass, a longer time window should be simulated to accurately compare the capability of each orbit to produce keys. Therefore, the satellite pass for the three different orbits over an entire year was modeled. Figure 14 below shows the yearly distilled key bits volume in the LEO, MEO, and GEO orbits. In the case of LEO, a volume of 285 Gbits was recorded under the given assumptions. For MEO and GEO, the volume of key bits produced was significantly lower, approximately one order of magnitude less, at 35.5 Gbits and 22 Gbits, respectively. This indicates that, even when using state-of-the-art equipment, LEO remains the preferred option over MEO and GEO. While MEO and GEO have distinct advantages and disadvantages, LEO currently appears to be the most promising orbit for space-to-Earth quantum communication. Improvements could potentially be achieved by using a larger aperture emitter on the satellite for MEO and GEO; however, this consideration is beyond the scope of this study.

The above KPIs allow key distillation rates with specified end-to-end loss budgets of approximately  $\sim 60$  dB, which offer QKD link implementations well beyond the current state-of-the-art commercially available systems offered by QKD vendors. More specifically, Toshiba and IDQ offer robust long-distance BB84 QKD system implementations operating at a 30 dB maximum link loss [81,82]. The difference between these commercially available systems (which report only link loss) and the reported results (which report end-to-end loss) in our study stems from the use of SNSPDs, which allow for increased detection efficiencies with lower jitter and low DCR detector noise. It has been shown that, when taking advantage of superconducting single-photon detectors optimized for QKD links, link efficiencies lower than  $10^{-6}$  can be supported [83]. Recently, Toshiba and Single Quantum



collaborated to enhance QKD transmission distances up to 300 km. They achieved this by integrating Single Quantum’s advanced SNSPDs, which offer high detection efficiency and low noise, thus effectively overcoming the signal loss over long fiber links [84].

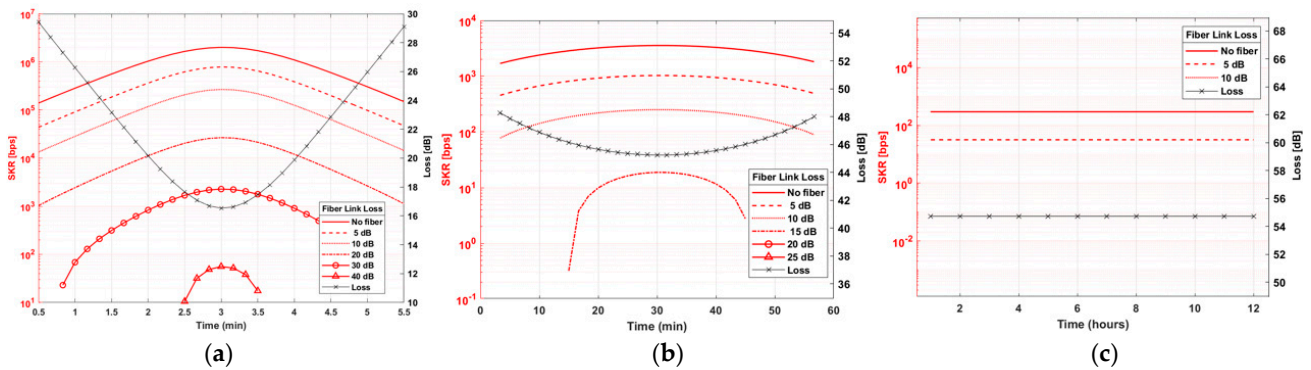


**Figure 13.** SKR over time accounting for the additional fiber distribution losses of  $D_{rx} = 2.3$  m with SNSPD detection and full-AO correction for (a) LEO, (b) MEO, and (c) GEO cases.

**Table 2.** Futuristic system assumptions.

Symbol	Parameter	Value
$f$	Emission rate	1 GHz
$N_t$	Transmitted block size	$10^{12}$ bits
$H_{sat}$	Satellite orbit altitude	550/8000/36,000 km
$D_{Rx}$	Rx telescope aperture diameter	2.28 m
$a$	Obscuration ratio	0.32
$f/x$	Focal ratio	$f/8$
$H_{OGS}$	OGS altitude	2300 m
$\sigma_p$	Pointing error variance	$0.7 \mu\text{rad}$
$C_n^2$	Refractive index structure parameter	$1.7 \times 10^{-14} \text{ m}^{-2/3}$
$H_{rad}$	Night-time Background solar radiance new moon	$1.5 \times 10^{-5} \text{ W/m}^2\text{sr} \mu\text{m}$
$t_{gate}$	Effective gate time window	0.5 ns

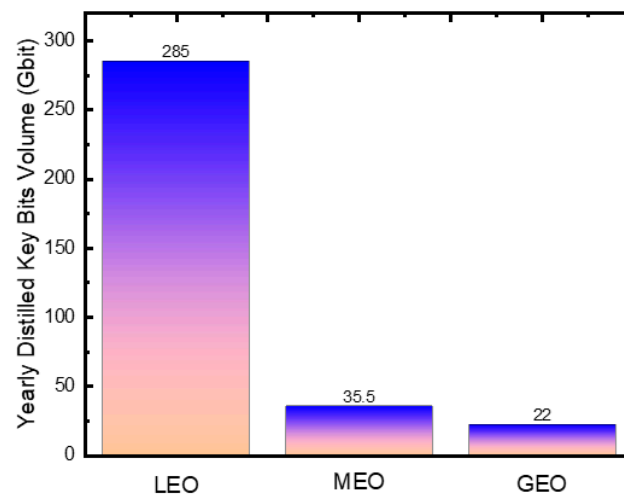


**Figure 14.** Yearly distilled key bit volume bar plot for LEO, MEO, and GEO.

Leveraging this deployment path of SNSPDs and the mature Wavelength Division Multiplexing (WDM) infrastructure, we suggest WDM-enabled, converged space/terrestrial system architectures for future satellite QKD links, which will offer robust and high-SKR QKD links. Figure 15 presents the proposed architecture, where multiple QKD sender stations operating with WDM-compatible weak coherent states feed polarization encoders



and intensity modulators before being multiplexed in a single optical beam emitted from the satellite telescope. By assuming the satellite is a trusted node, the WDM multiplexer can be considered as part of multiple QKD sender stations without introducing additional optical loss. Multiple WDM-enabled QKD links were collected from the same OGS before being demultiplexed in a low-loss, polarization-insensitive, and passive demultiplexer. The detection of single photons will be performed from superconducting nanowires sharing the same cryostat, thus allowing for a cost-effective solution for topologies where a large number of nanowires can be used in a centralized detection station. Time multiplexing techniques can also be considered in centralized detection stations in terms of further reducing the required number of SNSPDs in the proposed architecture. The use of fully synchronized electronic boards on the satellite payload feeding the WDM QKD sender stations facilitates the Alice/Bob synchronization steps that are required for the QBER estimation and post-processing in the centralized detection station based on SNSPD arrays. Since the WDM single-photon pulses are emitted from the same satellite, countermeasures against the polarization rotation due to satellite motion can be applied in the same way for different QKD links [85].

Beyond the system parameters considered in our study, additional system engineering parameters should also be considered for realizing deployable satellite–QKD downlinks. In polarization-encoded LEO satellite-to-ground QKD protocols, time-dependent rotations and static polarization transformations introduce additional errors. Hence, dynamic polarization tracking and compensation systems should be considered [86]. Experimental works on active polarization tracking and compensation system have recently showed the ultra-low QBER penalties associated with the polarization bases rotation, which occur due to the satellite’s motion [87]. In real QKD links, precise synchronization can also significantly increase the signal-to-noise ratio. In satellite QKD, synchronization is especially complicated due to such factors as signal fading, high loss, and the Doppler effect [88]. Synchronization can be implemented by leveraging a global navigation satellite system (GNSS) [73], but there are recent robust synchronization algorithms that have been successfully tested between the Micius satellite and OGSs [88]. In the latter experiment, it was shown that the selection of the appropriate synchronization methods can effectively decrease the QBER penalties associated with noise triggering. Besides the synchronization and polarization drift countermeasures, the amount of classical data that is required to be communicated between the satellite and ground station for implementing the key distillation process is also a critical parameter [30]. Laser communications can provide the required channel bandwidth to transmit all the relevant information, even within the temporal window of a single overpass of a LEO Cubesat [89].

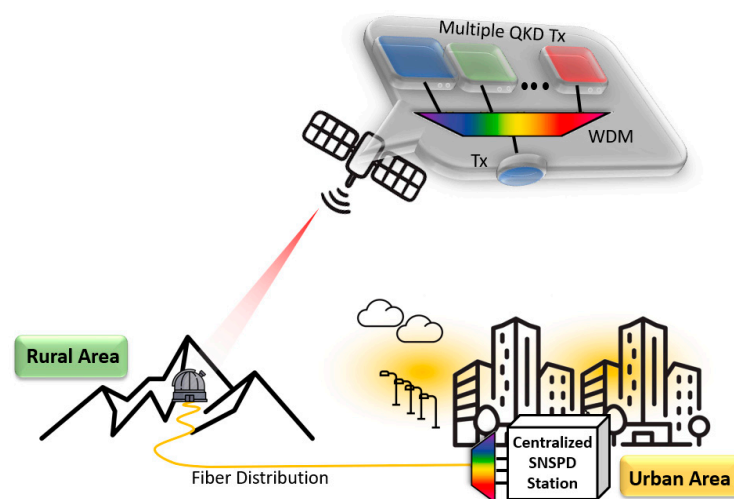


**Figure 15.** Multiple WDM-assisted, on-board QKD source architecture. The centralized SNSPD stations allowed for a significant boost in SKR.

## 6. Conclusions

In this work, a thorough analysis for satellite QKD downlinks was conducted, where the aim was to specify the system requirements for an operational satellite-to-ground QKD link under given atmospheric and system assumptions. In this study, an analysis for satellite DS-BB84 QKD downlinks was presented for a telecom C-band wavelength of 1550 nm. The specific requirements for implementing DS-BB84 QKD satellite-to-ground links with acceptable SKRs was discussed for various satellite orbits, QKD payload, and ground terminals specifications. System design parameters, including finite key size effects, atmospheric channel modeling, and quantum layer implementation parameters were considered. An evaluation of downlink scenarios at 1550 nm, focusing on link availability, on link budget, and secure key generation over time, was carried out. Emphasis was placed on the feasibility of distributing space photons through terrestrial fibers extension without the use of a trusted node in the OGS site, thus opening the door for converged space/terrestrial QCIs.

**Author Contributions:** Conceptualization, A.S., A.N., N.K.L. and G.G.; methodology, A.S., A.N., N.K.L. and G.G.; software, A.S., A.N. and N.K.L.; validation, A.S., A.N., N.K.L., G.G. and A.D.P.; formal analysis, A.S. and A.N.; investigation, A.S., A.N., N.K.L. and G.G.; resources, N.K.L., G.G. and H.A.; data curation, A.S. and A.N.; writing—original draft preparation, A.S., A.N., N.K.L. and G.G.; writing—review and editing, A.S., A.N., N.K.L., G.G. and A.D.P.; visualization, A.S. and A.N.; supervision, G.G., A.D.P. and H.A.; project administration, H.A.; funding acquisition, H.A. All authors have read and agreed to the published version of the manuscript.

**Funding:** This research was funded by the European’s Union Horizon Europe Research and Innovation Programme under project “Leap in Advancing of crItical Quantum key distribution-spAce components” (LaiQa, grant agreement no. 101135245).

**Institutional Review Board Statement:** Not applicable.

**Data Availability Statement:** The raw data supporting the conclusions of this article will be made available by the authors upon reasonable request.

**Acknowledgments:** This work was also supported in part by the European Commission through the project HellasQCI (under grant agreement no. 101091504) and by the European Union’s Horizon Europe Research and Innovation Programme under project “Quantum Security Networks Partnership” (QSNP, grant agreement no. 101114043). The views and opinions expressed are, however, those of the authors only and do not necessarily reflect those of the European Union. The European Union cannot be held responsible for them.

**Conflicts of Interest:** The authors declare no conflicts of interest.

## References

1. Wehner, S.; Elkouss, D.; Hanson, R. Quantum Internet: A Vision for the Road Ahead. *Science* **2018**, *362*, eaam9288. [[CrossRef](#)] [[PubMed](#)]
2. Long-Range QKD without Trusted Nodes Is Not Possible with Current Technology | Npj Quantum Information. Available online: <https://www.nature.com/articles/s41534-022-00613-4> (accessed on 11 April 2024).
3. Wallnöfer, J.; Hahn, F.; Wiesner, F.; Walk, N.; Eisert, J. Faithfully Simulating Near-Term Quantum Repeaters. *PRX Quantum* **2024**, *5*, 010351. [[CrossRef](#)]
4. de Forges de Parny, L.; Alibart, O.; Debaud, J.; Gressani, S.; Lagarrigue, A.; Martin, A.; Metrat, A.; Schiavon, M.; Troisi, T.; Diamanti, E.; et al. Satellite-Based Quantum Information Networks: Use Cases, Architecture, and Roadmap. *Commun. Phys.* **2023**, *6*, 12. [[CrossRef](#)]
5. Cuomo, D.; Caleffi, M.; Cacciapuoti, A.S. Towards a Distributed Quantum Computing Ecosystem. *IET Quantum Commun.* **2020**, *1*, 3–8. [[CrossRef](#)]
6. Cavaliere, F.; Prati, E.; Poti, L.; Muhammad, I.; Catuogno, T. Secure Quantum Communication Technologies and Systems: From Labs to Markets. *Quantum Rep.* **2020**, *2*, 80–106. [[CrossRef](#)]
7. Tenne, R.; Rossman, U.; Rephael, B.; Israel, Y.; Krupinski-Ptaszek, A.; Lapkiewicz, R.; Silberberg, Y.; Oron, D. Super-Resolution Enhancement by Quantum Image Scanning Microscopy. *Nat. Photon.* **2019**, *13*, 116–122. [[CrossRef](#)]
8. Ansari, V.; Brecht, B.; Gil-Lopez, J.; Donohue, J.M.; Řeháček, J.; Hradil, Z.; Sánchez-Soto, L.L.; Silberhorn, C. Achieving the Ultimate Quantum Timing Resolution. *PRX Quantum* **2021**, *2*, 010301. [[CrossRef](#)]

9. Liao, S.-K.; Cai, W.-Q.; Liu, W.-Y.; Zhang, L.; Li, Y.; Ren, J.-G.; Yin, J.; Shen, Q.; Cao, Y.; Li, Z.-P.; et al. Satellite-to-Ground Quantum Key Distribution. *Nature* **2017**, *549*, 43–47. [[CrossRef](#)] [[PubMed](#)]
10. Liao, S.-K.; Lin, J.; Ren, J.-G.; Liu, W.-Y.; Qiang, J.; Yin, J.; Li, Y.; Shen, Q.; Zhang, L.; Liang, X.-F.; et al. Space-to-Ground Quantum Key Distribution Using a Small-Sized Payload on Tiangong-2 Space Lab. *Chin. Phys. Lett.* **2017**, *34*, 090302. [[CrossRef](#)]
11. Jones, A. China Is Developing a Quantum Communications Satellite Network. SpaceNews, 10 March 2023. Available online: <https://spacenews.com/china-is-developing-a-quantum-communications-satellite-network/> (accessed on 23 June 2024).
12. Khmelev, A.; Duplinsky, A.; Bakhshaliev, R.; Ivchenko, E.; Pismeniuk, L.; Mayboroda, V.; Nesterov, I.; Chernov, A.; Trushechkin, A.; Kiktenko, E.; et al. Eurasian-Scale Experimental Satellite-Based Quantum Key Distribution with Detector Efficiency Mismatch Analysis. *Opt. Express* **2024**, *32*, 11964. [[CrossRef](#)]
13. Yin, J.; Cao, Y.; Li, Y.-H.; Liao, S.-K.; Zhang, L.; Ren, J.-G.; Cai, W.-Q.; Liu, W.-Y.; Li, B.; Dai, H.; et al. Satellite-Based Entanglement Distribution over 1200 Kilometers. *Science* **2017**, *356*, 1140–1144. [[CrossRef](#)] [[PubMed](#)]
14. Ren, J.-G.; Xu, P.; Yong, H.-L.; Zhang, L.; Liao, S.-K.; Yin, J.; Liu, W.-Y.; Cai, W.-Q.; Yang, M.; Li, L.; et al. Ground-to-Satellite Quantum Teleportation. *Nature* **2017**, *549*, 70–73. [[CrossRef](#)] [[PubMed](#)]
15. EAGLE-1: Advancing Europe’s Leadership in Quantum Communications | SES. Available online: <https://www.ses.com/newsroom/eagle-1-advancing-europes-leadership-quantum-communications> (accessed on 11 April 2024).
16. SAGA for Quantum Key Distribution. Available online: [https://www.esa.int/ESA\\_Multimedia/Images/2019/04/SAGA\\_for\\_quantum\\_key\\_distribution](https://www.esa.int/ESA_Multimedia/Images/2019/04/SAGA_for_quantum_key_distribution) (accessed on 11 April 2024).
17. Tricco, G. The Upcoming of Iris2: Bridging the Digital Divide and Strengthening the Role of the EU in International Space Law. *J. Law. Mark. Innov.* **2023**, *2*, 17–42. [[CrossRef](#)]
18. Hutterer, M.; Auer, M.; Baliuka, A.; Marquardt, C.; Weinfurter, H.; Gall, M.; Günther, K.; Moll, F.; Papadopoulos, C.; Pudelko, J.; et al. QUBE-II—Quantum Key Distribution with a CubeSat. In Proceedings of the 73rd International Astronautical Congress, IAC 2022, Paris, France, 18–22 September 2022.
19. Peev, M.; Pacher, C.; Alléaume, R.; Barreiro, C.; Bouda, J.; Boxleitner, W.; Debuisschert, T.; Diamanti, E.; Dianati, M.; Dynes, J.F.; et al. The SECOQC Quantum Key Distribution Network in Vienna. *New J. Phys.* **2009**, *11*, 075001. [[CrossRef](#)]
20. García Cid, M.I.; Ortiz Martín, L.; Martín Ayuso, V. Madrid Quantum Network: A First Step to Quantum Internet. In Proceedings of the 16th International Conference on Availability, Reliability and Security, Vienna, Austria, 17–20 August 2021; Association for Computing Machinery: New York, NY, USA; pp. 1–7.
21. Ribezzo, D.; Zahidy, M.; Vagniluca, I.; Biagi, N.; Francesconi, S.; Occhipinti, T.; Oxenløwe, L.K.; Lončarić, M.; Cvitić, I.; Stipčević, M.; et al. Deploying an Inter-European Quantum Network. *Adv. Quantum Technol.* **2023**, *6*, 2200061. [[CrossRef](#)]
22. Brauer, M.; Vicente, R.J.; Buruaga, J.S.; Méndez, R.B.; Braun, R.-P.; Geitz, M.; Rydlichowski, P.; Brunner, H.H.; Fung, F.; Peev, M.; et al. Linking QKD Testbeds across Europe. *Entropy* **2024**, *26*, 123. [[CrossRef](#)] [[PubMed](#)]
23. Qin, H.; Haw, J.Y.; Duan, X.; Cai, Y.; Murthy, R.; Ng, N.; Sikdar, B.; Kurtsiefer, C.; Kasper, M.; Ling, A. The National Quantum-Safe Network in Singapore. In Proceedings of the 49th European Conference on Optical Communications (ECOC 2023), Glasgow, UK, 1–5 October 2023; Volume 2023, pp. 1294–1297.
24. Scott, A.; Jennewein, T.; Cain, J.; D’Souza, I.; Higgins, B.; Hudson, D.; Podmore, H.; Soh, W. The QEYSSAT Mission: On-Orbit Demonstration of Secure Optical Communications Network Technologies. In Proceedings of the Environmental Effects on Light Propagation and Adaptive Systems III, Online, 21–25 September 2020; SPIE: Bellingham, WA, USA, 2020; Volume 11532, pp. 71–76.
25. Mazzarella, L.; Lowe, C.; Lowndes, D.; Joshi, S.K.; Greenland, S.; McNeil, D.; Mercury, C.; Macdonald, M.; Rarity, J.; Oi, D.K.L. QUARC: Quantum Research Cubesat—A Constellation for Quantum Communication. *Cryptography* **2020**, *4*, 7. [[CrossRef](#)]
26. Lenart, A.; Sivasankaran, S.; Hidding, B.; Oi, D.; Ling, A.; Neilson, P. CubeSat In-Orbit Validation of in Situ Performance by High Fidelity Radiation Modelling. *arXiv* **2022**, arXiv:2209.00408.
27. Ahmadi, N.; Schwertfeger, S.; Werner, P.; Wiese, L.; Lester, J.; Da Ros, E.; Krause, J.; Ritter, S.; Abasifard, M.; Cholsuk, C.; et al. QUICK3<sup>3</sup>—Design of a Satellite-Based Quantum Light Source for Quantum Communication and Extended Physical Theory Tests in Space. *Adv. Quantum Technol.* **2024**, *7*, 2300343. [[CrossRef](#)]
28. Gündoğan, M.; Sidhu, J.S.; Henderson, V.; Mazzarella, L.; Wolters, J.; Oi, D.K.L.; Krutzik, M. Proposal for Space-Borne Quantum Memories for Global Quantum Networking. *npj Quantum Inf.* **2021**, *7*, 128. [[CrossRef](#)]
29. Luo, W.; Li, Y.; Li, Y.; Tao, X.; Han, L.; Cai, W.; Yin, J.; Ren, J.; Liao, S.; Peng, C. Intrinsically Stable 2-GHz Polarization Modulation for Satellite-Based Quantum Key Distribution. *IEEE Photonics J.* **2022**, *14*, 1–6. [[CrossRef](#)]
30. Roger, T.; Singh, R.; Perumangatt, C.; Marangon, D.G.; Sanzaro, M.; Smith, P.R.; Woodward, R.I.; Shields, A.J. Real-Time Gigahertz Free-Space Quantum Key Distribution within an Emulated Satellite Overpass. *Sci. Adv.* **2023**, *9*, ead5873. [[CrossRef](#)] [[PubMed](#)]
31. Home—QUDICE. Available online: <https://qudice.eu/> (accessed on 11 April 2024).
32. Press Release—LaiQa Project. Available online: <https://www.Laiqa-Horizon.Eu/Press-Release/> (accessed on 23 June 2024).
33. Bonato, C.; Tomaello, A.; Da Deppo, V.; Naletto, G.; Villorosi, P. Feasibility of Satellite Quantum Key Distribution. *New J. Phys.* **2009**, *11*, 045017. [[CrossRef](#)]
34. Ntanos, A.; Lyras, N.K.; Zavitsanos, D.; Giannoulis, G.; Panagopoulos, A.D.; Avramopoulos, H. LEO Satellites Constellation-to-Ground QKD Links: Greek Quantum Communication Infrastructure Paradigm. *Photonics* **2021**, *8*, 544. [[CrossRef](#)]
35. Scriminich, A.; Foletto, G.; Picciariello, F.; Stanco, A.; Vallone, G.; Villorosi, P.; Vedovato, F. Optimal Design and Performance Evaluation of Free-Space Quantum Key Distribution Systems. *Quantum Sci. Technol.* **2022**, *7*, 045029. [[CrossRef](#)]

36. Ntanos, A.; Lyras, N.; Zavitsanos, D.; Anwar, S.; Alia, O.; Giannoulis, G.; Kanellos, G.; Panagopoulos, A.; Avramopoulos, H. MEO Satellite-to-Ground Decoy-State QKD Links Realistic Performance Analysis. In Proceedings of the International Conference on Space Optics—ICSO 2022, Dubrovnik, Croatia, 3–7 October 2022; SPIE: Bellingham, WA, USA, 2023; Volume 12777, pp. 1116–1130.
37. Ntanos, A.; Lyras, N.K.; Stathis, A.; Giannoulis, G.; Panagopoulos, A.D.; Avramopoulos, H. Satellite-to-Ground QKD in Urban Environment: A Comparative Analysis of Small-Sized Optical Ground Stations. *IEEE Aerosp. Electron. Syst. Mag.* **2024**, *39*, 16–29. [[CrossRef](#)]
38. Acosta, V.M.; Dequal, D.; Schiavon, M.; Montmerle-Bonnefois, A.; Lim, C.B.; Conan, J.-M.; Diamanti, E. Analysis of Satellite-to-Ground Quantum Key Distribution with Adaptive Optics. *New J. Phys.* **2024**, *26*, 023039. [[CrossRef](#)]
39. Polnik, M.; Mazzarella, L.; Di Carlo, M.; Oi, D.K.; Riccardi, A.; Arulselvan, A. Scheduling of Space to Ground Quantum Key Distribution. *EPJ Quantum Technol.* **2020**, *7*, 3. [[CrossRef](#)]
40. How to Choose the Best QKD Network Technology: Three Different Satellite Based Scenarios Compared. Available online: [https://www.spiedigitallibrary.org/conference-proceedings-of-spie/11852/2599218/How-to-choose-the-best-QKD-network-technology--three/10.1117/12.2599218.full#\\_=\\_](https://www.spiedigitallibrary.org/conference-proceedings-of-spie/11852/2599218/How-to-choose-the-best-QKD-network-technology--three/10.1117/12.2599218.full#_=_) (accessed on 11 April 2024).
41. Sidhu, J.S.; Brougham, T.; McArthur, D.; Pousa, R.G.; Oi, D.K.L. Finite Key Effects in Satellite Quantum Key Distribution. *npj Quantum Inf.* **2022**, *8*, 18. [[CrossRef](#)]
42. Exciting News for the Greek Connectivity Optical Ground Stations—Raymetrics. 2024. Available online: <https://raymetrics.com/wp-content/uploads/2024/01/Hardware-Newsletter-KOM1.pdf> (accessed on 23 June 2024).
43. Rattenbury, N.J.; Ashby, J.; Bennet, F.; Birch, M.; Cater, J.E.; Ferguson, K.; Giggenbach, D.; Grant, K.; Knopp, A.; Knopp, M.T.; et al. Update on the German and Australasian Optical Ground Station Networks. *arXiv* **2024**, arXiv:2402.13282.
44. Liao, S.-K.; Yong, H.-L.; Liu, C.; Shentu, G.-L.; Li, D.-D.; Lin, J.; Dai, H.; Zhao, S.-Q.; Li, B.; Guan, J.-Y.; et al. Long-Distance Free-Space Quantum Key Distribution in Daylight towards Inter-Satellite Communication. *Nat. Photon.* **2017**, *11*, 509–513. [[CrossRef](#)]
45. Marsden, M.A.; Downey, J.N.; Tedder, S.A.; Vyhnalek, B.E. Testing of A Photon-Counting Optical Ground Receiver with Emulated Space-to-Ground Link Effects. In Proceedings of the SPIE Photonics West Free-Space Laser Communications XXXVI, San Francisco, CA, USA, 30–31 January 2024.
46. Makarov, V.; Abrikosov, A.; Chaiwongkhot, P.; Fedorov, A.K.; Huang, A.; Kiktenko, E.; Petrov, M.; Ponomova, A.; Ruzhitskaya, D.; Tayduganov, A.; et al. Preparing a Commercial Quantum Key Distribution System for Certification against Implementation Loopholes. *arXiv* **2023**, arXiv:2310.20107.
47. Vasylyev, D.; Vogel, W.; Moll, F. Satellite-Mediated Quantum Atmospheric Links. *Phys. Rev. A* **2019**, *99*, 053830. [[CrossRef](#)]
48. Bourgoin, J.-P.; Meyer-Scott, E.; Higgins, B.L.; Helou, B.; Erven, C.; Hübel, H.; Kumar, B.; Hudson, D.; D’Souza, I.; Girard, R.; et al. A Comprehensive Design and Performance Analysis of Low Earth Orbit Satellite Quantum Communication. *New J. Phys.* **2013**, *15*, 023006. [[CrossRef](#)]
49. Gruneisen, M.T.; Eickhoff, M.L.; Newey, S.C.; Stoltenberg, K.E.; Morris, J.F.; Bareian, M.; Harris, M.A.; Oesch, D.W.; Olike, M.D.; Flanagan, M.B.; et al. Adaptive-Optics-Enabled Quantum Communication: A Technique for Daytime Space-To-Earth Links. *Phys. Rev. Appl.* **2021**, *16*, 014067. [[CrossRef](#)]
50. Lu, C.-Y.; Cao, Y.; Peng, C.-Z.; Pan, J.-W. Micius Quantum Experiments in Space. *Rev. Mod. Phys.* **2022**, *94*, 035001. [[CrossRef](#)]
51. Li, Y.-H.; Li, S.-L.; Hu, X.-L.; Jiang, C.; Yu, Z.-W.; Li, W.; Liu, W.-Y.; Liao, S.-K.; Ren, J.-G.; Li, H.; et al. Free-Space and Fiber-Integrated Measurement-Device-Independent Quantum Key Distribution under High Background Noise. *Phys. Rev. Lett.* **2023**, *131*, 100802. [[CrossRef](#)] [[PubMed](#)]
52. Ansys STK | Digital Mission Engineering Software. Available online: <https://www.ansys.com/products/missions/ansys-stk> (accessed on 18 April 2024).
53. Andrews, L.C.; Phillips, R.L. *Laser Beam Propagation through Random Media*, 2nd ed.; SPIE Press: Bellingham, WA, USA, 2005; ISBN 978-0-8194-5948-0.
54. Kiasaleh, K. On the Probability Density Function of Signal Intensity in Free-Space Optical Communications Systems Impaired by Pointing Jitter and Turbulence. *Opt. Eng.* **1994**, *33*, 3748–3757. [[CrossRef](#)]
55. ITU-R. *Propagation Data and Prediction Methods Required for the Design of Earth-Space Telecommunication Systems*; ITU-R 206/3; International Telecommunication Union: Geneva, Switzerland, 2015.
56. Bufton, J.L. Comparison of Vertical Profile Turbulence Structure with Stellar Observations. *Appl. Opt.* **1973**, *12*, 1785–1793. [[CrossRef](#)]
57. Kaushal, H.; Kaddoum, G. Optical Communication in Space: Challenges and Mitigation Techniques. *IEEE Commun. Surv. Tutor.* **2017**, *19*, 57–96. [[CrossRef](#)]
58. Giggenbach, D.; Moll, F. Scintillation Loss in Optical Low Earth Orbit Data Downlinks with Avalanche Photodiode Receivers. In Proceedings of the 2017 IEEE International Conference on Space Optical Systems and Applications (ICSOS), Naha, Japan, 14–16 November 2017; pp. 115–122. [[CrossRef](#)]
59. Marsili, F.; Verma, V.B.; Stern, J.A.; Harrington, S.; Lita, A.E.; Gerrits, T.; Vayshenker, I.; Baek, B.; Shaw, M.D.; Mirin, R.P.; et al. Detecting Single Infrared Photons with 93% System Efficiency. *Nat. Photon.* **2013**, *7*, 210–214. [[CrossRef](#)]
60. Er-long, M.; Zheng-fu, H.; Shun-sheng, G.; Tao, Z.; Da-sheng, D.; Guang-can, G. Background Noise of Satellite-to-Ground Quantum Key Distribution. *New J. Phys.* **2005**, *7*, 215. [[CrossRef](#)]
61. Tyson, R.K.; Frazier, B.W. *Principles of Adaptive Optics*, 5th ed.; CRC Press: Boca Raton, FL, USA, 2022; ISBN 978-1-00-314019-1.



62. Jovanovic, N.; Schwab, C.; Guyon, O.; Lozi, J.; Cvetojevic, N.; Martinache, F.; Leon-Saval, S.; Norris, B.; Gross, S.; Doughty, D.; et al. Efficient Injection from Large Telescopes into Single-Mode Fibres: Enabling the Era of Ultra-Precision Astronomy. *Astron. Astrophys.* **2017**, *604*, A122. [[CrossRef](#)]
63. Bonnefois, A.M.; Velluet, M.-T.; Cissé, M.; Lim, C.B.; Conan, J.-M.; Petit, C.; Sauvage, J.-F.; Meimon, S.; Perrault, P.; Montri, J.; et al. Feasibility Demonstration of AO Pre-Compensation for GEO Feeder Links in a Relevant Environment. *Opt. Express* **2022**, *30*, 47179–47198. [[CrossRef](#)]
64. Chai, G.; Huang, P.; Cao, Z.; Zeng, G. Suppressing Excess Noise for Atmospheric Continuous-Variable Quantum Key Distribution via Adaptive Optics Approach. *New J. Phys.* **2020**, *22*, 103009. [[CrossRef](#)]
65. Cao, Y.; Li, Y.-H.; Yang, K.-X.; Jiang, Y.-F.; Li, S.-L.; Hu, X.-L.; Abulizi, M.; Li, C.-L.; Zhang, W.; Sun, Q.-C.; et al. Long-Distance Free-Space Measurement-Device-Independent Quantum Key Distribution. *Phys. Rev. Lett.* **2020**, *125*, 260503. [[CrossRef](#)]
66. Oliker, M.D.; Gruneisen, M.T. How Much Value Does Adaptive Optics Add to a Satellite QKD Uplink? In Proceedings of the Quantum Technologies and Quantum Information Science V, Strasbourg, France, 9–12 September 2019; SPIE: Bellingham, WA, USA, 2019; Volume 11167, pp. 10–19.
67. TOMCAT. Available online: <https://artes.esa.int/projects/tomcat> (accessed on 24 March 2023).
68. Ruilier, C. A Study of Degraded Light Coupling into Single-Mode Fibers. In Proceedings of the Astronomical Interferometry, Kona, HI, USA, 20–28 March 1998; SPIE: Bellingham, WA, USA, 1998; Volume 3350, pp. 319–329.
69. Gruneisen, M.T.; Sickmiller, B.A.; Flanagan, M.B.; Black, J.P.; Stoltenberg, K.E.; Duchane, A.W. Adaptive Spatial Filtering for Daytime Satellite Quantum Key Distribution. In Proceedings of the Emerging Technologies in Security and Defence II; and Quantum-Physics-based Information Security III, Amsterdam, The Netherlands, 22–25 September 2014; SPIE: Bellingham, WA, USA, 2014; Volume 9254, pp. 7–20.
70. Gruneisen, M.T.; Flanagan, M.B.; Sickmiller, B.A. Modeling Satellite-Earth Quantum Channel Downlinks with Adaptive-Optics Coupling to Single-Mode Fibers. *Opt. Eng.* **2017**, *56*, 126111. [[CrossRef](#)]
71. Krzic, A.; Heinig, D.; Goy, M.; Steinlechner, F. Dual-Downlink Quantum Key Distribution with Entangled Photons: Prospects for Daylight Operation. In Proceedings of the Dual-Downlink Quantum Key Distribution with Entangled Photons: Prospects for Daylight Operation; International Conference on Space Optics, Dubrovnik, Croatia, 3–7 October 2022.
72. Dikmelik, Y.; Davidson, F.M. Fiber-Coupling Efficiency for Free-Space Optical Communication through Atmospheric Turbulence. *Appl. Opt.* **2005**, *44*, 4946–4952. [[CrossRef](#)]
73. Schmitt-Manderbach, T.; Weier, H.; Fürst, M.; Ursin, R.; Tiefenbacher, F.; Scheidl, T.; Perdigues, J.; Sodnik, Z.; Kurtsiefer, C.; Rarity, J.G.; et al. Experimental Demonstration of Free-Space Decoy-State Quantum Key Distribution over 144 Km. *Phys. Rev. Lett.* **2007**, *98*, 010504. [[CrossRef](#)] [[PubMed](#)]
74. Ma, X.; Qi, B.; Zhao, Y.; Lo, H.-K. Practical Decoy State for Quantum Key Distribution. *Phys. Rev. A* **2005**, *72*, 012326. [[CrossRef](#)]
75. Lucamarini, M.; Patel, K.A.; Dynes, J.F.; Fröhlich, B.; Sharpe, A.W.; Dixon, A.R.; Yuan, Z.L.; Penty, R.V.; Shields, A.J. Efficient Decoy-State Quantum Key Distribution with Quantified Security. *Opt. Express* **2013**, *21*, 24550–24565. [[CrossRef](#)] [[PubMed](#)]
76. Song, T.-T.; Qin, S.-J.; Wen, Q.-Y.; Wang, Y.-K.; Jia, H.-Y. Finite-Key Security Analyses on Passive Decoy-State QKD Protocols with Different Unstable Sources. *Sci. Rep.* **2015**, *5*, 15276. [[CrossRef](#)] [[PubMed](#)]
77. Eraerds, P.; Walenta, N.; Legré, M.; Gisin, N.; Zbinden, H. Quantum Key Distribution and 1 Gbps Data Encryption over a Single Fibre. *New J. Phys.* **2010**, *12*, 063027. [[CrossRef](#)]
78. Bellei, F.; Cartwright, A.P.; McCaughan, A.N.; Dane, A.E.; Najafi, F.; Zhao, Q.; Berggren, K.K. Free-Space-Coupled Superconducting Nanowire Single-Photon Detectors for Infrared Optical Communications. *Opt. Express* **2016**, *24*, 3248–3257. [[CrossRef](#)] [[PubMed](#)]
79. Mueller, A.S.; Korzh, B.; Runyan, M.; Wollman, E.E.; Beyer, A.D.; Allmaras, J.P.; Velasco, A.E.; Craiciu, I.; Bumble, B.; Briggs, R.M.; et al. Free-Space Coupled Superconducting Nanowire Single-Photon Detector with Low Dark Counts. *Optica* **2021**, *8*, 1586–1587. [[CrossRef](#)]
80. Tamura, Y.; Sakuma, H.; Morita, K.; Suzuki, M.; Yamamoto, Y.; Shimada, K.; Honma, Y.; Sohma, K.; Fujii, T.; Hasegawa, T. The First 0.14-dB/Km Loss Optical Fiber and Its Impact on Submarine Transmission. *J. Light. Technol.* **2018**, *36*, 44–49. [[CrossRef](#)]
81. Clavis XG QKD System. Available online: <https://www.idquantique.com/quantum-safe-security/products/clavis-xg-qkd-system/> (accessed on 26 July 2023).
82. Long Distance QKD System LD—Toshiba Quantum Key Distribution. Toshiba Quantum Technology. Available online: <https://www.toshiba.eu/quantum/products/quantum-key-distribution/long-distance-qkd-system-ld/> (accessed on 23 June 2024).
83. Boaron, A.; Boso, G.; Rusca, D.; Vulliez, C.; Autebert, C.; Caloz, M.; Perrenoud, M.; Gras, G.; Bussièrès, F.; Li, M.-J.; et al. Secure Quantum Key Distribution over 421 Km of Optical Fiber. *Phys. Rev. Lett.* **2018**, *121*, 190502. [[CrossRef](#)] [[PubMed](#)]
84. Toshiba Europe and Single Quantum Partner to Provide Extended Long-Distance QKD Deployment Capability. Toshiba Quantum Technology. Available online: <https://www.toshiba.eu/quantum/news/toshiba-europe-and-single-quantum-partner-to-provide-extended-long-distance-qkd-deployment-capability/> (accessed on 23 June 2024).
85. Influence of Satellite Motion on Polarization Qubits in a Space-Earth Quantum Communication Link. Available online: <https://opg.optica.org/oe/fulltext.cfm?uri=oe-14-21-10050&id=116342> (accessed on 22 April 2024).
86. Toyoshima, M.; Takenaka, H.; Shoji, Y.; Takayama, Y.; Takeoka, M.; Fujiwara, M.; Sasaki, M. Polarization-Basis Tracking Scheme in Satellite Quantum Key Distribution. *Int. J. Opt.* **2011**, *2011*, e254154. [[CrossRef](#)]



87. Khanna, A.; Sakhiya, P.V.; Bhatt, J.B.; Jain, A.; Kumar, M.S.; Singh, D.K. Development of Active Polarization Tracking and Compensation System for Satellite-to-Ground QKD. In Proceedings of the 2023 IEEE Microwaves, Antennas, and Propagation Conference (MAPCON), Ahmedabad, India, 11–14 December 2023; pp. 1–6.
88. Miller, A.V. Time Synchronization in Satellite Quantum Key Distribution. *Probl. Inf. Transm.* **2023**, *59*, 225–238. [[CrossRef](#)]
89. Li, L.; Xuejiao, Z.; Jianhua, Z.; Changzhi, X.; Yi, J. Advanced Space Laser Communication Technology on CubeSats. *ZTE Commun.* **2020**, *18*, 45–54. [[CrossRef](#)]

**Disclaimer/Publisher’s Note:** The statements, opinions and data contained in all publications are solely those of the individual author(s) and contributor(s) and not of MDPI and/or the editor(s). MDPI and/or the editor(s) disclaim responsibility for any injury to people or property resulting from any ideas, methods, instructions or products referred to in the content.